Faceted 3D Supercrystals for Plasmonic Photocatalysis: Design, Reactivity and Operando Studies

Charlène Brissaud, Wajdi Chaâbani, Jesús Giráldez-Martínez, Meyssa Mockbel, Eva Yazmin Santiago, Jaime Gabriel Trazo, Rahul Nag, Stéphanie Lau-Truong, Gaëlle Blond, Marco Faustini, et al.

Faceted 3D Supercrystals for Plasmonic Photocatalysis: Design, Reactivity and Operando Studies

Charlène Brissaud, Wajdi Chaâbani, Jesús Giráldez-Martínez, Meyssa Mockbel, Eva Yazmin Santiago, Jaime Gabriel Trazo, Rahul Nag, Stéphanie Lau-Truong, Gaëlle Blond, Marco Faustini, Cyrille Hamon, Lucas V. Besteiro, Jean-Yves Piquemal, Miguel Comesaña-Hermo**

Charlène Brissaud, Wajdi Chaâbani, Meyssa Mockbel, Rahul Nag, Stéphanie Lau-Truong, Jean-Yves Piquemal, Miguel Comesaña-Hermo
Université Paris Cité, CNRS, ITODYS, 75006 Paris (France)
E-mail: charlene.brissaud@gmail.com, miguel.comesana-hermo@u-paris.fr

Jesús Giráldez-Martínez, Eva Yazmin Santiago, Lucas V. Besteiro
CINBIO, Universidade de Vigo, Department of Physical Chemistry, 36310 Vigo (Spain)

Jaime Gabriel Trazo, Cyrille Hamon
Université Paris-Saclay, CNRS, Laboratoire de Physique des Solides, 91405 Orsay (France)

Gaëlle Blond
Université de Strasbourg, CNRS, Laboratoire d'Innovation Thérapeutique, 67000 Strasbourg (France)

Marco Faustini
Sorbonne Université, CNRS, UMR 7574, Chimie de la Matière Condensée de Paris,75005 Paris (France)

Marco Faustini
Institut Universitaire de France (IUF), 75231 Paris (France)

Keywords: plasmonic photocatalysis, 3D supercrystals, self-assembly, organic transformations, operando SERS

Abstract

Solar-driven plasmonic photocatalysis has emerged as a powerful tool to enhance chemical reactivity, improving the efficiency and selectivity in a large number of transformations. Plasmonic nanoparticles are often implemented in photocatalysis as colloidal dispersions but they face issues related to the reduced photoactivation of the metallic surface in concentrated solutions and poor long-term colloidal stability. To overcome these limitations, we introduce 3D plasmonic supercrystals created through the depletion- and evaporation-induced self-assembly of metal nanoparticles as novel heterogeneous plasmonic photocatalysts. They present large electromagnetic field enhancements associated to the formation of regular arrays of plasmonic hot spots, leading to improved chemical reactivities through the generation of hot charge carriers. To demonstrate this, we chose two challenging organic transformations, an oxidative polymerization and different C–C cross-coupling reactions, that can be activated by modifying the chemical composition of the assemblies. The anisotropic shapes of the building blocks lead to the formation of 3D supercrystals exposing different surfaces. Importantly, by performing *operando* Surface-Enhanced Raman Spectroscopy at the single supercrystal level, we unveil the surface-dependent reactivity of each individual plasmonic superstructure. Our combined experimental and theoretical approach provides with key insights into structure-function correlations and offers guidelines for the rational design of versatile supercrystal photocatalysts.

1. Introduction

Plasmonic photocatalysis holds the potential to drive chemical reactivity with an unprecedented control over efficiency and selectivity.[1] Such unique photocatalytic features derive from the generation of non-thermalized charge carriers and high electromagnetic field enhancements in noble metal nanoparticles (NPs) under localized surface plasmon resonance (LSPR) excitation.[2] Over more than one decade, plasmonic photocatalysis has been implemented to drive a large variety of chemical processes, including organic transformations, the activation of small molecules for the production of renewable fuels and the growth/etching of inorganic nanostructures.[2–7] Many of the studies reported to date implement plasmonic NPs as colloidal solutions whose catalytic performances are highly dependent on the surface area of the material exposed to irradiation and available to interact with a given molecular species. Unfortunately, several experimental issues can have a negative impact on their efficiency. For instance, the photodesorption of the stabilizing ligands can cause the aggregation of the objects, resulting in loss of colloidal stability and subsequent deterioration of their optical and photocatalytic features.[8,9] In order to overcome such limitations, the rational assembly of plasmonic NPs into larger structures has been recently postulated as an alternative approach for their use as heterogeneous photocatalysts. In this way, self-assembled superstructures can be exploited as heterogeneous catalysts with improved chemical features related to their collective properties, such as the large electromagnetic field enhancements obtained through the generation of interparticle hot spots.[10–12]

A recent report by Cortés and coworkers describes the use of binary 2D superlattices ~~as antenna-reactor systems~~ formed by the assembly of spherical Au and Pt NPs as outstanding catalysts for the photo-induced generation of H_2 from formic acid.[13] In these structures, the specific disposition of ultra-small Pt NPs at the hot spots generated between neighbor Au resonators leads to an increase in the catalytic activity of the former upon plasmonic excitation through an energy transfer process. Another recent work describes the implementation of self-assembled monolayers of Ag nano-octahedra for the photocatalytic conversion of N_2 into NH_3.[14] Here, hot electron injection is at the origin of the enhanced catalytic activity, while the specific organization of the NPs within the superlattices (square versus hexagonal arrangement) has a strong effect on their final features due to the different intensities of the electromagnetic field enhancements produced. These two examples evidence the advantages associated to the implementation of 2D assemblies of plasmonic objects over extended surfaces, producing improved activities and prolonged stabilities with respect to colloidal dispersions.

3D plasmonic supercrystals (SCs) are versatile platforms in which the symmetry, lattice spacing, crystal habit and shape can be easily modulated by simply changing the individual building blocks and the assembly processes implemented, resulting in tailored optical properties.[15] In this manner, 3D SCs have been used as highly sensitive and adaptable sensing platforms due to their high density of hot spots, even for the detection of analytes with low affinities for the plasmonic component.[16,17] We believe that such adaptability can be implemented for the development of a rich chemical reactivity in which the collective properties of the SCs can provide with extra degrees of freedom to modulate efficiency and selectivity. Along these lines, 3D arrangements lead to the exposition of different surfaces and hence, the catalytic activity derived from them can be modified through the rational control of the assembly process.[18] Moreover, by simply modulating the chemical composition of the plasmonic resonators, one can target a vast number of chemical reactions, including a plethora of organic transformations.[4,19,20] These features, together with their ability to generate exotic crystallographic patterns by simply modulating the size and shape of their building blocks,[21–23] confer 3D plasmonic SCs with the potential to become a new class of versatile photocatalytic platforms. For instance, Lemineur and coworkers have recently implemented 3D SCs composed by spherical core-shell Ag@Pt NPs as photocatalysts for the hydrogen evolution reaction.[24] Unfortunately, fast erosion and corrosion of these materials occurred under photocatalytic conditions due to the presence of defects at the crystalline interface between the two metals.

In the present work we report on the use of 3D plasmonic SCs made by the self-assembly of noble metal nanorods (NRs) as heterogeneous photocatalytic platforms for organic reactions driven by sunlight. Here, the chemical composition of the individual objects has been tuned, allowing the activation of different organic transformations. Such assembly process leads to the formation of two different orientations of the NRs with respect to the substrate, each exposing different surfaces with varying optical features, electromagnetic field intensities and spatial patterns. These differences produce distinct efficiencies for specific photochemical processes. In order to study the surface-dependent properties of these materials, we have followed their reactivity at the single SC level and in *operando* conditions by means of Surface-Enhanced Raman Spectroscopy (SERS). The experimental data obtained is complemented by simulations on the optical response and surface electron dynamics of the assemblies, leading to structure-function correlations. Together, these findings show the promising properties of plasmonic SCs for photocatalytic applications while providing insights into the roles of composition, plasmonic coupling and SCs orientation in determining their performances.

2. Results and Discussion

Plasmonic NRs have been synthesized following established seed-mediated growth protocols with some modifications (for more details, please refer to the Materials and Methods section).[25,26] Pentatwinned (PTW) Au NRs have been chosen instead of single-crystalline ones given their low polydispersities and convenient manipulation of their aspect ratios,[25] while also permitting the deposition of an homogeneous Pd shell for the formation of core-shell Au@Pd NRs.[26] Accordingly, Au NRs presenting an aspect ratio of 4.4 (**Figures S1** and **S3** in the Supporting Information) have been implemented for the photo-oxidation of an organic substrate.[4] In the case of the core-shell NRs, we will take advantage of the catalytic properties of Pd in C–C cross-coupling reactivity.[27] Given that the plasmonic properties of Pd are relatively poor due to the large imaginary part of its dielectric function in the visible and NIR regions, the thickness of the Pd layer has been kept as thin as possible in order to minimize damping of the original plasmonic signature from the Au NRs. This method enables the formation of a well-defined Pd shell with a thickness of ca. 10 nm on the tips and 2 nm on the sides, with a final aspect ratio of 4.4 (see **Figures S2a-c** and **S3**). Even though the deposition of the Pd shell alters the optical properties of the materials, Au@Pd NRs still display a plasmonic response in the visible and NIR regions (**Figure S2d**), hence potentially exhibiting photocatalytic features under solar radiation.

Both Au and Au@Pd 3D SCs have been obtained via evaporation-induced self-assembly by drop-casting concentrated colloidal solutions of NRs on glass or silicium substrates as schematized in **Figure S4**. For this, we have taken advantage of the interplay between depletion forces and electrostatic interactions, enabling tuning of the SC structure by varying experimental parameters such as temperature, humidity or depletant concentration.[28,29] This approach leads to the formation of micron-sized assemblies of NRs for both compositions (**Figure 1**). As can be observed in the SEM images, the size of the crystalline domains in the Au SCs is always larger than that of the Au@Pd assemblies. Such difference may come from inhomogeneities in the Pd shell, as surface roughness can affect negatively the depletion attraction between the NPs and their assembly.[30,31] The presence of cetyltrimethylammonium-based micelles in suspension (either CTAC or CTAB have been chosen as depletants) generates an attraction force between the NRs. As the solvent evaporates, electrostatic repulsion weakens progressively due to charge screening, which combined with the increasing strength of depletion forces, leads to the formation of SCs. Two distinct orientations can be observed in both samples, with the NRs parallel or perpendicular with respect to the substrate on the outer

or center part of the deposit, respectively (**Figure 1a, d**). Such behavior has been previously reported by other authors for the assembly of Au@Ag NRs.[32,33] The different dispositions patterns might be explained by the so-called coffee ring effect.[34] During the drying process, liquid evaporating from the edge is replenished by liquid from the interior inducing a flow which could orient the SCs.[35] In line with this, we found the SCs to be radially oriented on average at the edge of the deposit, while the SCs towards the center are randomly scattered on the substrate (**Figure 1 a, d**). The resulting SCs consist in 3D arrays of NRs lying horizontally with respect to the substrate that can attain thicknesses close to 1 μm (**Figure 1b, e** for Au and Au@Pd, respectively). At the center of the deposit, all SCs consist of NRs standing on the substrate, composed of 2-3 vertically-stacked monolayers.[36] SEM images of these deposits show the pentagonal cross-section of the metal NRs within assemblies of trapezoidal shapes (**Figure 1c, f**).

Small-Angle X-ray Scattering (SAXS) characterization of the deposits demonstrates the presence of a hexagonal arrangement both at the center and at the edge of the samples (**Figure 1 g, i**). Interestingly, SAXS curves taken at the edge of the deposit present additional Bragg peaks consistent with the parallel orientation of the NRs with respect to the substrate. Moreover, Fast Fourier Transforms (FFTs) were performed on the SEM micrographs of the vertically standing assemblies and confirmed the hexagonal ordering of the NRs for both the Au and Au@Pd SCs (**Figure 1h, j**). Hexagonal packing is usually observed in SCs made of NRs with single-crystalline structures.[37] It has been proven experimentally that the spontaneous assembly of Au@Ag NRs with pentagonal cross-sections leads to ice-ray and Dürer packings with rectangular symmetry, together with other intermediate polymorphs from these two configurations.[23] The fact that we do not observe such crystallographic arrangement but rather a hexagonal packing, as evidenced by SAXS and electron microscopy, is likely due to the small diameter of the NRs and the presence of capping ligands, resulting in an effective circular cross-section of the building blocks.

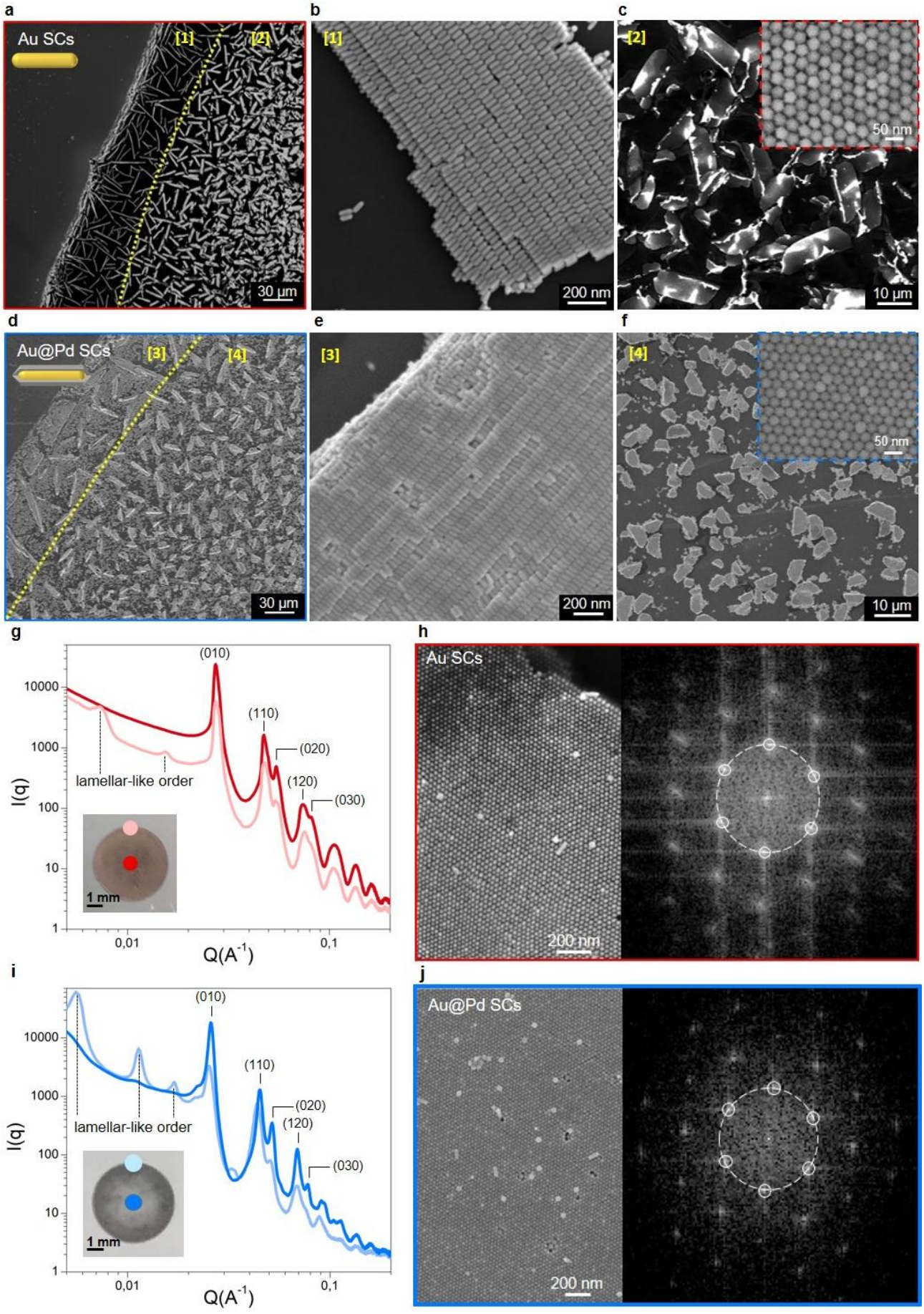
a
Au SCs
[1]
[2]
30 µm
b
[1]
200 nm
c
[2]
50 nm
10 µm
d
Au@Pd SCs
[3]
[4]
30 µm
e
[3]
200 nm
f
[4]
50 nm
10 µm
g
(010)
(110)
(020)
(120)
(030)
lamellar-like order
I(q)
10000
1000
100
10
1
1 mm
0,01
0,1
Q(A-1)
h
Au SCs
200 nm
i
(010)
(110)
(020)
(120)
(030)
lamellar-like order
I(q)
10000
1000
100
10
1
1 mm
0,01
0,1
Q(A-1)
j
Au@Pd SCs
200 nm

Figure 1. a, d) SEM images of the edge of Au (a, red) and Au@Pd (d, blue) deposits. b, e) and c, f) Enlarged SEM images of regions [1;3] and [2;4] showing horizontally and vertically standing assemblies of NRs, respectively. The insets in c) and f) show the pentagonal cross-section of the Au and Au@Pd NRs constituting the SCs. g, i) SAXS spectra of the Au an Au@Pd SCs taken at different positions of the deposit as indicated in the insets. h, j) SEM images and corresponding FFTs of standing Au and Au@Pd NR SCs, respectively.

The optical properties of the SCs have been characterized using hyperspectral imaging with a dark-field microscope in reflection mode, enabling optical mapping with sub-micrometric resolution. In this vein, the scattering spectra of an ensemble of Au and Au@Pd SCs are presented in **Figure S5**, showcasing a broad response within the visible and NIR regions of the spectrum. Moreover, scattering spectra obtained for both Au and Au@Pd SCs at the single SC level are presented in **Figure 2**. Firstly, we compared the optical signatures at the single SC level for a given conformation. Our results show the excitation of different plasmon modes of the SCs, depending on the relative orientation of the NRs within the assemblies. For instance, Au@Pd SCs with vertically-aligned NRs display a broad band centered at 728, 692 and 682 nm for SCs i, ii and iii, respectively (**Figure 2a**). In contrast, when studying their lying counterpart, the spectra red-shifted, with the maxima at 846, 843 and 834 nm for iv, v and vi SCs, respectively (**Figure 2b**). These measurements are in agreement with the orientation of the NRs in the assemblies with the lying SCs displaying a noticeable red-shift (ca. 140 nm) of the plasmon modes compared to standing SCs. Moreover, the optical response for a given orientation are very similar in terms of width, intensity and position of the bands across the sample, indicating SCs uniformity. Such characteristic is a major advantage for characterizing the photocatalytic features of the samples at the single SC level and *in operando* conditions (vide infra). Changing the chemical composition of the NRs also has an important impact on the optical features of the SCs. The plasmon band of a standing Au@Pd SC is broaden and red-shifted compared to that of an Au SC in the same configuration, the former being a direct consequence of the lossy character of Pd in the visible and NIR (**Figure 2c**). These results demonstrate that both Au and Au@Pd SCs exhibit optical properties in the visible-NIR range. Moreover, photocatalytic ensemble experiments in solution will provide insight into their potential as efficient plasmonic photocatalysts, which is likely related to strong absorption contributions.

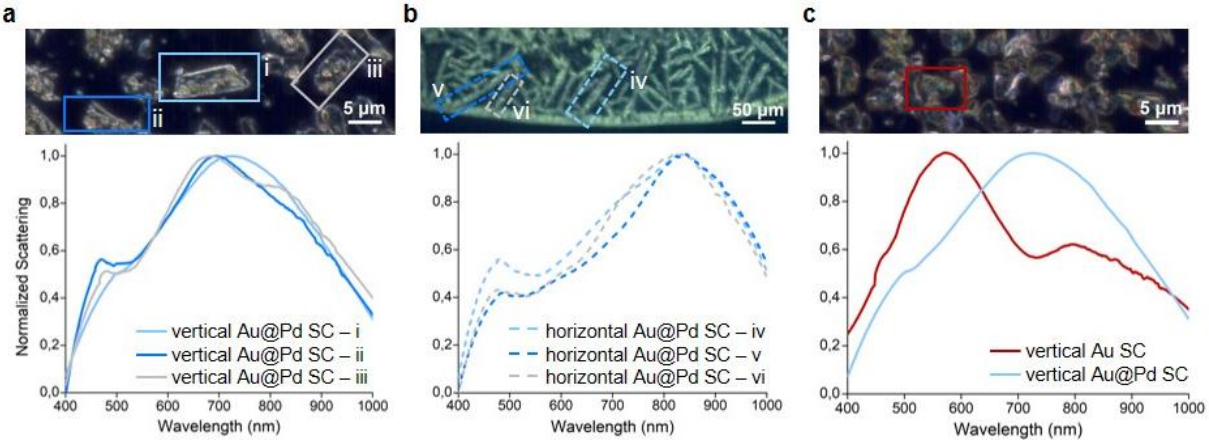

Figure 2. Hyperspectral images (top) and corresponding scattering spectra (bottom) of a) Au@Pd SCs made from vertically-aligned NRs, b) Au@Pd SCs made from horizontally-aligned NRs and c) Au and Au@Pd SCs made from vertically-aligned NRs. The rectangles in the optical images of the top panel show the analyzed assemblies.

Once the structural and optical features of the SCs were fully characterized, we probed their photocatalytic capabilities to drive organic transformations. In the particular case of Au SCs, we targeted a model oxidation reaction, given the ability of this metal to generate activated O_2 species under irradiation.[38] Accordingly, we have investigated the photocatalytic properties of Au SCs for the oxidative polymerization of aniline into polyaniline (PANI), a challenging transformation that is usually produced from the chemical oxidative polymerization of the monomer in a strong acidic solution and using an oxidant (e.g., ammonium persulfate) to initiate the reaction.[39–41] We conducted the experiments at room temperature under O_2 atmosphere, using dimethylsulfoxide (DMSO) as solvent, in the presence of the Au SCs and under irradiation with a solar simulator during 72 hours (**Figure 3a**). In these conditions, a gradual change of color was observed, with the aniline solution turning from colorless to orange (**Figure S6a**). The reaction mixture was analyzed by gas chromatography coupled to mass spectrometry (GC-MS), revealing 90 % conversion of aniline. Importantly, no reactivity could be observed when the same reaction was performed in the dark. This and other control experiments (for more details, see the SI), together with the experimental conditions used, allow us to discard any relevant role played by photothermal effects in the photocatalytic activity observed.[42]

When randomly deposited PTW Au NRs (also referred to as non-organized) were used as photocatalysts, only 36 % of the aniline was consumed in the same reaction time (**Figure 3b**). We thus conclude that the higher photocatalytic efficiency of the Au SCs is due to the formation of plasmonic inter-particle hot spots in these structures. More precisely, the resulting

enhancement of the electric field at the surface of the SCs increases the generation of hot charge carriers, improving the catalytic activity of the materials.[43] This result is particularly interesting given that the Au SCs present a drastically lower amount of catalytic surface sites available with respect to the non-assembled photocatalyst in which a deposit of mostly randomly oriented Au NRs is observed on the substrate (**Figure S7a**). Following this, fine-tuning the 3D supercrystals to produce thinner structures could result in increased active surface areas and an overall enhancement in catalytic efficiency. Additionally, the recyclability of the catalyst has been also studied since the use of Au SCs deposited on a glass slide enables its facile recovery from the reaction medium. It is worth noting here that the SCs remained attached on the substrate during the reaction without any leaching of plasmonic objects into the solution. Interestingly, the conversion rate of aniline (≥ 80 %) remains high after 5 catalytic cycles (**Figure 3c**), demonstrating the validity of our approach to form stable and reusable heterogeneous photocatalysts.

The absorption spectrum of the reaction mixture was recorded and compared to the spectra of other potential reaction products in dimethylsulfoxide (DMSO), such as nitrobenzene or azobenzene (**Figure S6b**).[44] Since no match could be found for any of these species and their signatures were not detected by chromatography techniques, we conclude that they are not produced in our experiments, highlighting the selectivity of the photochemical process. The overall aspect of the reaction mixture spectrum (sharp peak at 254 nm, broad and less intense peak at 330 nm and small absorption between 425 and 525 nm) coincides with the absorption spectrum of polyaniline (PANI) synthesized under microwave irradiation of an aniline solution.[45] HRTEM images of the post-catalytic reaction mixture show the presence of a dense network of pseudo-spherical NPs with crystalline domains ranging between ca. 5 and 20 nm (**Figure S6c**). The distances measured from the electron diffraction patterns of these NPs can be indexed to the atomic distances of the emeraldine form of PANI according to a pseudo-orthorhombic indexation (**Figure S6c**).[46] Hence, GC-MS, absorption spectroscopy and HRTEM demonstrate that the Au SCs enable the oxidation of aniline under simulated solar irradiation, leading to its polymerization under mild conditions. Importantly, the transformation of aniline is accompanied by the concomitant oxidation of DMSO into dimethyl sulfone ($DMSO_2$) (**Figure 3d**). This finding suggests the presence of reactive oxygen species (ROS) in our reaction medium through the interaction between the photogenerated charge carriers and oxygen molecules[42,47,48] towards the formation of $DMSO_2$, which is likely to be the species responsible for the polymerization of aniline. On one hand, the fundamental role played by the

ROS has been confirmed by performing the same photocatalytic experiment in the presence of 2,2,6,6-tetramethylpiperidine 1-oxyl (TEMPO), a well-known ROS scavenger. Accordingly, the presence of this molecule leads to a very large decrease of the photocatalytic activity (11.7 % vs. 90 % of aniline oxidation) by shutting down the oxidative relay triggered by the plasmonic charge carriers that is responsible for the oxidation of the solvent (**Figure S8**). On the other, the lack of reactivity observed when the reaction is performed in other solvents such as cyclohexane or ethanol instead of DMSO also supports the hypothesis that $DMSO_2$ works as a primer allowing the polymerization reaction to take place (**Figure S9**).

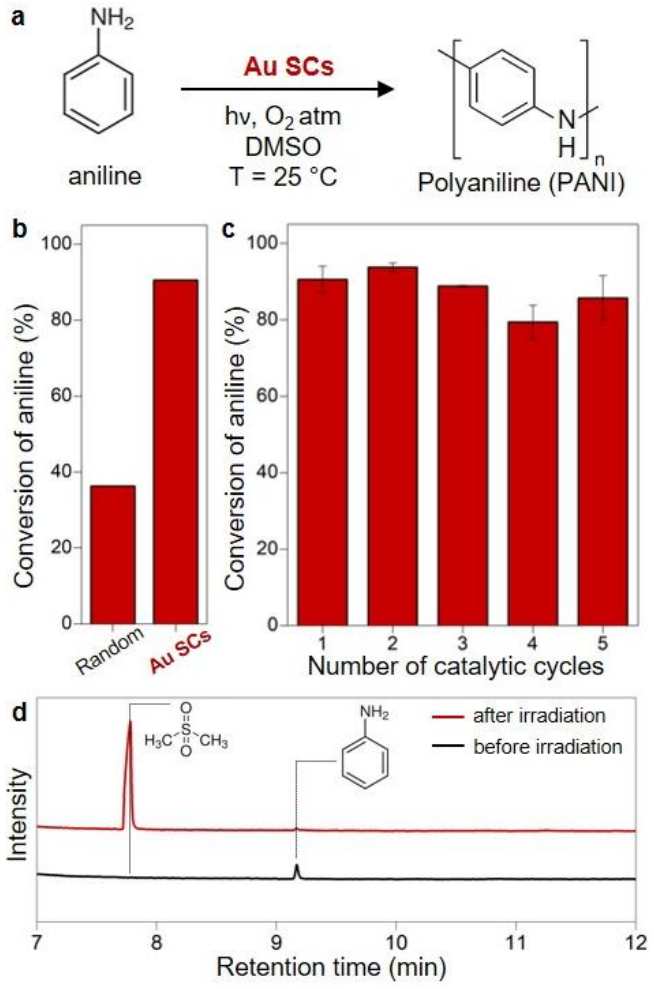

Figure 3. a) Aniline oxidation reaction under standard photocatalytic conditions. b) Photocatalytic activities of different catalysts for the reaction performed under O_2 atmosphere and at 25 °C for 72 h. c) Recyclability tests of Au SCs for 5 photocatalytic cycles. d) Gas chromatographs of the reaction medium before and after the reaction.

In order to study the photocatalytic activity of Au@Pd SCs we have chosen the Stille reaction, a cross-coupling process widely used in organic synthesis that involves the interaction between

an organohalide and an organostannane using a Pd(0)-catalyst, usually a Pd-bearing phosphine ligand in homogeneous conditions.[49,50] Accordingly, we investigated the photocatalytic performance of Au@Pd SCs for the Stille coupling between bromobenzene (BB) and tributyl(vinyl) tin (TBVT) in toluene at 90 °C, leading to styrene as cross-coupling product (**Figure 4a**). After 24 hours of irradiation under these conditions we observe the conversion of 66 % of styrene (**Figure 4b**). For comparison, when the same reaction is repeated using a deposit of non-organized Au@Pd NRs (same volume and concentration) in comparison with the SCs (**Figure S7b**), the production of styrene was found to be of 40 %, leading to a 40 % decrease with respect to the organized Au@Pd SCs (**Figure 4b**). As previously discussed for the oxidative polymerization of aniline in the presence of Au SCs, the higher photocatalytic efficiency of the regular assemblies compared to randomly deposited NRs is the result of the strong electromagnetic hot spots present in the former and the subsequent improvement of hot charge carrier densities generated under continuous illumination. Again, it is important to remember that the SCs present a much smaller surface-to-volume ratio of exposed active metal, highlighting the important underestimation of the improved activity observed in the Au@Pd SCs with respect to the random deposits. Moreover, the hydrophilic nature of the Au@Pd NRs impedes their use as colloidal photocatalysts under these particular reaction conditions without a tedious post-synthetic surface functionalization process with hydrophobic ligands. Conversely, when the reaction is performed in the dark with external heating at 90 °C as the sole energy input to activate the cross-coupling reaction, only a negligible quantity of styrene is produced (**Figure 4c**). This result indicates that the efficiency of the coupling under our experimental conditions can be attributed to non-thermal plasmonic effects generated upon irradiation of the SCs, rather than external heating.

Unexpectedly, benzaldehyde (BA) and benzyl alcohol (BOH) are also produced in a significant amount under irradiation (**Figure 4c**). Since these products are usually obtained at the industrial scale through chlorination of toluene and subsequent hydrolysis, we investigated how they can be formed under in this reaction. To do so, we performed the same photocatalytic process without the organostannane compound (**Figure 4c**). Given that both BA and BOH are produced under these conditions, hence without the generation of styrene, we hypothesize that the two by-products stem from the oxidation of toluene upon irradiation. Likewise, monitoring the products formed during the early stages of the reaction demonstrates that these two species do not derive from the oxidation of styrene, given that their formation does not lead to a concomitant transformation of the latter (**Figure S10**). Such findings are also confirmed by the

fact that BA and BOH are not produced when the reaction occurs in the presence of the two coupling agents in the dark (**Figure 4c**). A plausible explanation for the oxidation of toluene can be the introduction of an oxidant in the reaction medium, as it has already been reported by Shoukat and coworkers.[51] As for aniline oxidation, the presence of ROS is directly related to the formation of hot charge carriers under plasmonic excitation. To assess the importance of these transient species, the Stille coupling has been carried out in the presence of TEMPO. In these conditions, only styrene is produced (**Figure 4c**), confirming that ROS are responsible for the oxidation of toluene into BA and BOH. Nonetheless, the presence of TEMPO also leads to a significant decrease in the production of styrene (34 % of the expected quantity), suggesting that such ROS may also play a role in the cross-coupling reaction.

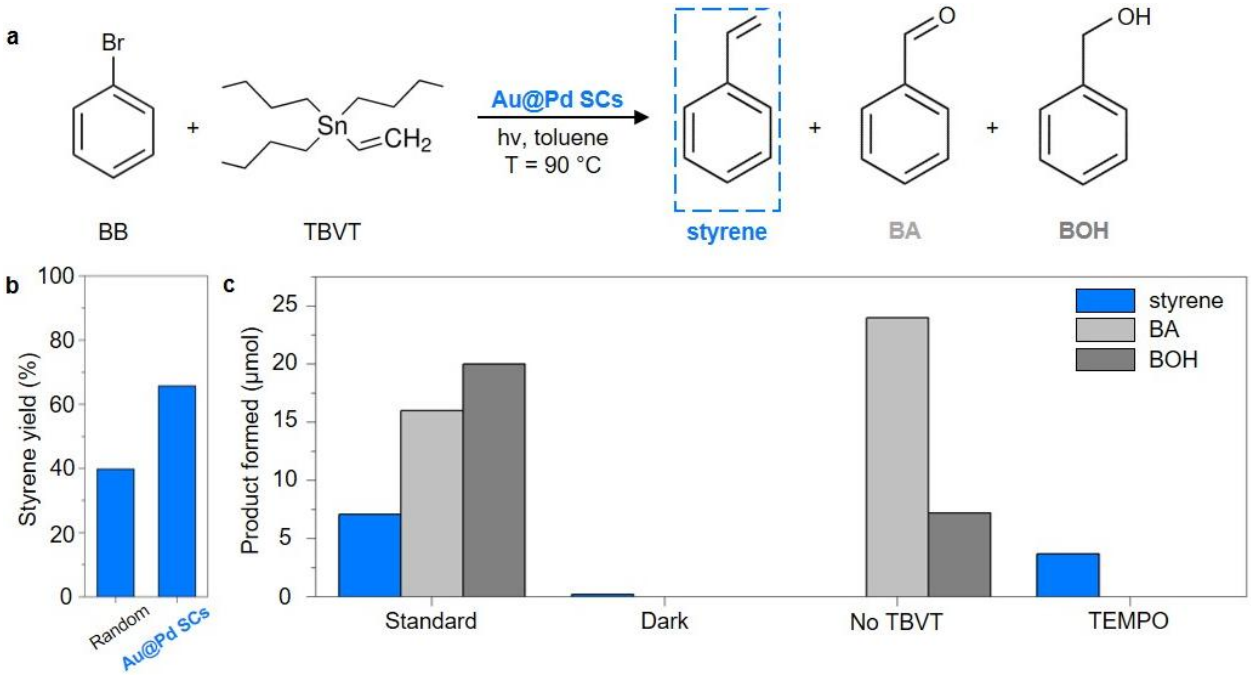

Figure 4. a) Stille cross-coupling reaction under standard photocatalytic conditions. b) Photocatalytic activities of different photocatalysts for the reaction performed under air atmosphere at 90 °C for 24 h. c) Quantification of the different products obtained when performing the Stille coupling at 90 °C for 24 h under different experimental conditions. The standard conditions correspond to the use of air atmosphere and irradiation. No TBVT means that only BB is used as reagent. TEMPO indicates that the experiment is carried out in presence of the ROS inhibitor.

While we showed that the photoreactivity can be boosted by using faceted SCs, the surface-dependent reactivity of these assemblies remains an open question. To address this aspect, a second cross-coupling reaction was monitored by using *operando* SERS[52–54] and at the single

supercrystal level by using Au@Pd SCs as heterogeneous photocatalysts. To do so, solutions of 4-bromothiophenol (4-BTP) and m-tolylboronic acid (TBA) were drop-casted sequentially onto the Au@Pd SCs in order to ensure a saturation of the available surface with the targeted molecules. Subsequently, these materials were irradiated with a 633 nm laser to induce the coupling while recording SERS spectra (**Figure 5a**). Thanks to the small diameter of the laser beam (ca. 1 μm), we can precisely target a specific portion within a SC among the hundreds forming the deposit. In this manner, the influence of the relative orientation of the NRs constituting the SC, i.e. lying horizontally vs. standing vertically on the substrate, with respect to the laser beam on the reactivity of the photocatalyst can be monitored. The SERS spectra recorded at different reaction times on horizontal Au@Pd SCs are shown in **Figure 5b**. The first spectrum (light grey) shows the vibrational fingerprint of 4-BTP on the SCs, with the characteristic peaks at 1076 cm^{-1} (ring deformation), 1181 cm^{-1} (C–H deformation) and 1556 cm^{-1} (C–C stretching).[55] Upon prolonged laser irradiation, an asymmetric broadening of the 1556 cm^{-1} peak due to the appearance of a shoulder around 1580–1600 cm^{-1} is observed, as depicted in the black spectrum of **Figure 5b**. The latter signal can be assigned to the cross-coupling product, 3'-methyl-4-mercapto-biphenyl (MMBP) (**Figure S11**).[56] By measuring the intensity ratio between the 1580–1600 cm^{-1} and 1556 cm^{-1} peaks over time (referred to as $I_{product}$ / $I_{reactant}$), we are able to study the kinetics of the cross-coupling reaction at the single SC level. Accordingly, the $I_{product}$ / $I_{reactant}$ ratio has been obtained at different times of the reaction for both types of Au@Pd SCs (**Figure 5c**), as represented in **Figure 5d**. Depending on the exposed surface of the SCs, very different reaction kinetics are observed. Indeed, when the reaction is performed on standing NRs (dark blue), the intensity ratio slightly increases over time to a value of 0.2 after 160 s of irradiation. In contrast, for the reaction carried out on NRs lying horizontally and prone to tip-to-tip longitudinal coupling (light blue), the intensity ratio increases steeply to 0.9 in 120 s and then reaches a plateau. For comparison purposes, when Au SCs are used instead of Au@Pd, very sluggish reaction kinetics are observed for the transformation of 4-BTP, suggesting a very inefficient coupling between these molecules even for much longer irradiation times (**Figure S12**). This result emphasizes the fundamental role played by the thin Pd layer and the secondary role played by thermal effects in this reactivity. In order to demonstrate the broad validity of the surface-dependent reactivity of the SCs, similar experiments have been performed for the oxidative dimerization of 4-aminothiophenol (4-ATP) immobilized onto Au SCs towards the formation of 4,4'-dimercaptoazobenzene (DMAB).[57] Faster reaction kinetics are also observed for horizontal SCs of Au NRs with respect to the vertical ones (**Figure S13**).

In order to obtain further insight into our experimental findings, we performed calculations to compute the generation rates of hot charge carriers for both dispositions of the Au@Pd SCs onto the substrate, implementing the quantum formalism developed by Govorov and coworkers.[58,59] The model system is based in a hexagonal arrangement of Au@Pd NRs whose dimensions are in accordance with the experimental data (see the Materials and Methods section for further details). The simulations show that when the entire surface of the NRs within the SCs is taken into consideration, the vertical ones present the highest generation of hot charge carriers of the two arrangements, in contrast to our experimental results (**Figure S14**). As discussed previously in this work, we believe that the surface of the NRs located in the interior of the SC are not accessible to the molecular substrates, hence limiting the catalytic activity of these structures to the most superficial plasmonic layers. Consequently, we analyzed the computational data considering the penetration depth of the reagents along the z-axis (taken perpendicular to the substrate), parametrizing the generation rate of hot electrons ($Rate_{HE}$, see Supplementary Information for the description of the formalism modelling surface assisted hot carrier excitation) as a function of maximum penetration along this axis. In particular, we highlight the results for values of $|\Delta z|$ that correspond only to the surface of the first layer of NRs that is directly exposed to the environment, with a penetration depth of 13 nm for the vertical SCs and 23 nm for the horizontal ones (**Figure 5e**). In this scenario, the relative importance of the computed hot electron generation efficiency among the two dispositions is reversed, as the highest population is obtained for the horizontal SCs (**Figure 5f**). Strikingly, when the relative rates of excitation are compared with the experimental ratios of the chemical transformation obtained via SERS after 160 s of irradiation, i.e. once the plateau is reached, we observe a very strong agreement between theory and experiment (3.92 vs. 4.43, respectively) (**Figure 5g**). The differences in the photocatalytic profiles between horizontal and vertical SCs suggest that the efficiency of the reaction depends on the intensity and spatial accessibility of the interparticle plasmonic hot spots, as previously postulated. Along these lines, electromagnetic field enhancement maps of both configurations show the strong inter-particle coupling achieved in both geometries (**Figure S15-S16**). When considering only the topmost surface, the strong tip-to-tip hot spots in the horizontal SC, as well as the staged arrangement resulting from the close packing of the NRs, produce the strongest photocatalytic enhancement. As discussed before, hot spots induce a higher rate of carriers that leads to improved photocatalytic activities.[43] The vertical arrangement would be an advantageous configuration, per unit area, if all the interstitial spaces could be exploited in driving the reaction, but presents the intrinsic difficulty of having an inversely proportional relationship between the interparticle

spacing, which allows free reagent flow, and hot spot enhancement, which drives the chemical process more efficiently. A recent work by Cortés and coworkers demonstrates the dominance of plasmonic hot spots over preferential adsorption of a given molecular substrate onto specific crystalline surface as main parameter driving plasmon induced photocatalysis.[60]

Theoretical studies have allowed us to take into consideration the impact of the number of NR layers forming the SCs in their ability to generate hot charge carriers. As shown in **Figure S17a**, the surface-averaged hot electron generation rate for horizontally stacked Au@Pd NRs exhibits two distinct maxima corresponding to systems composed of 2 and 6 layers. A similar trend is observed in the spatial evolution of the surface-integrated electromagnetic field enhancement integrated along xy planes (**Figure S17b**), which also shows maximum intensities at the same layer numbers within the 23 nm penetration depth used to define the accessible reactive area when computing the hot electron excitation rates. Near-field enhancement maps for SCs with varying NR layer numbers are presented in **Figure S17c**, also highlighting notable differences in the intensity and distribution of plasmonic hot spots across the surface. Such findings show that fine tuning the thickness of the SC would permit an unprecedented control of the density of charge carriers generated. It is important to note that these results have been obtained under the premise that reactivity is confined to the outermost surface of the Au@Pd SCs. If reactivity within the full volume of the assemblies were considered, thus accounting for enhanced molecular diffusivity of organic substrates, different trends might emerge, underscoring the potential of designing 3D plasmonic assemblies with improved porosity for optimized photocatalytic performances.

We have also performed simulations in order to exclude thermal contribution as the main parameter driving the photo-reactivity observed during *operando* SERS experiments. For this, we have implemented the same multi-layer geometric model used to compute the generation of charge carriers (**Figure S18a**). Solving the heat transfer equation, in otherwise identical conditions, the vertical configuration achieves a higher surface temperature than the horizontal one, in opposition to the kinetics obtained experimentally. Even when studying a deeper stack of NRs (12 layers) and selecting the optimal polarization we find similar temperatures than the two layer SC with vertically-oriented NRs (**Figure S18b**).

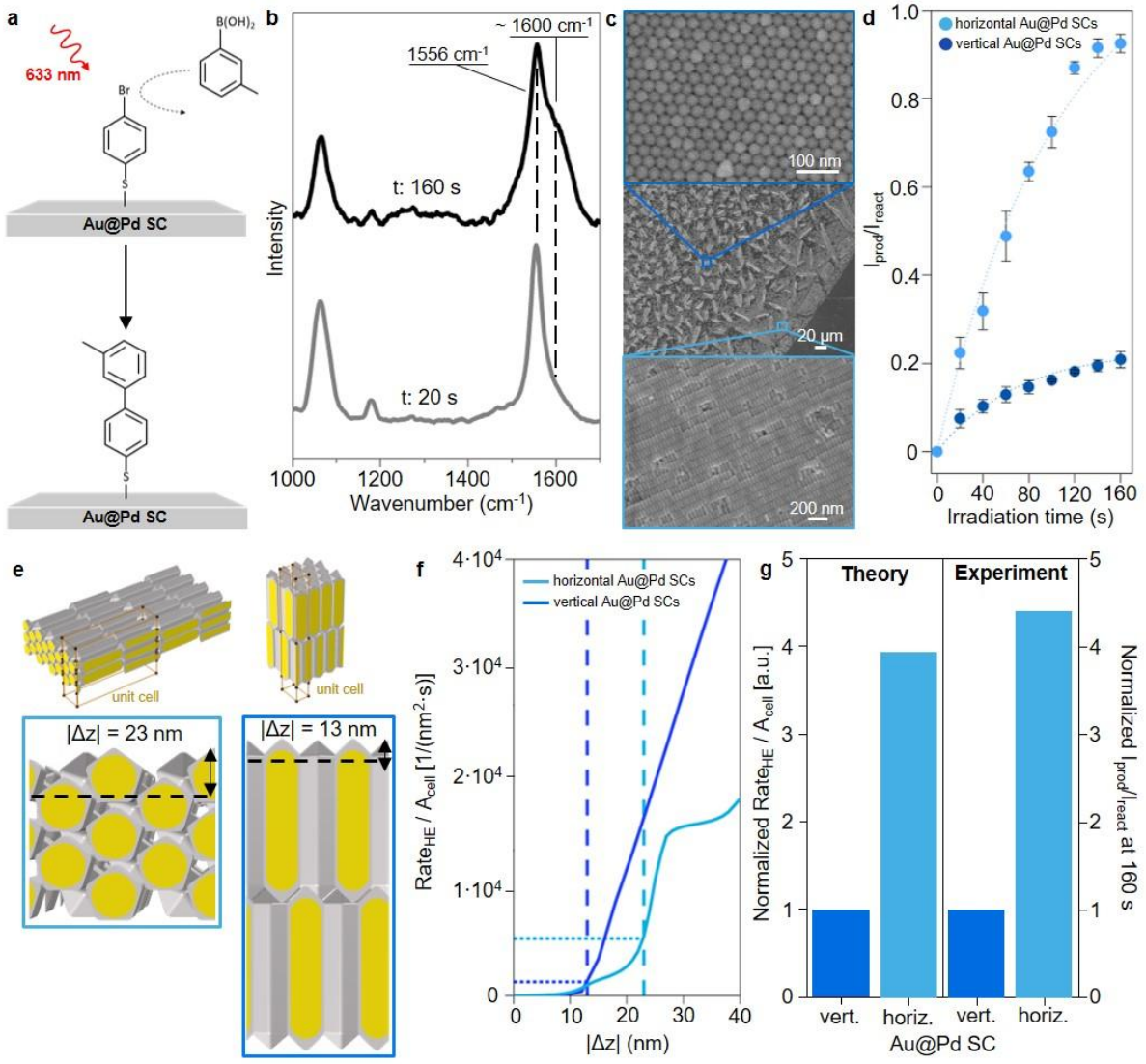

Figure 5. a) Schematic representation of the reaction at the surface of an Au@Pd SC. b) SERS spectra recorded on a horizontal Au@Pd SC at different irradiation times. c) SEM images of the edge of a deposit with the top and bottom panels showing the vertical (dark blue) or horizontal (light blue) assemblies, respectively. d) Photocatalytic activities of the Au@Pd SCs depending on the relative disposition with respect to the substrate and under *operando* SERS. Irradiation conditions: λ_{exc}: 633 nm, 100x obj., 0.76 mW power + 20 s acquisition time. (e) 3D models used for the simulation of the optical spectra and generation of hot charge carriers. The zoom-ins present the unit cells and the penetration depth of the first monolayer for the horizontal (23 nm) and vertical (13 nm) SCs. f) Theoretical generation rates of hot electrons as a function of the penetration depth in the SCs along the z-axis (normal to the irradiation). g) Comparison of the normalized hot electron generation rates and the normalized experimental reactivity for operando SERS at 160 s for the vertical (dark blue) and horizontal (light blue) Au@Pd SCs.

3. Conclusions

This study highlights the significant potential of 3D plasmonic SCs made from self-assembled noble metal NRs as effective heterogeneous photocatalysts for organic reactions. The anisotropic nature of the objects and their arrangement into ordered assemblies play a crucial role in enhancing photocatalytic performance, as demonstrated by the efficient polymerization of aniline and the cross-coupling reactions enabled by these materials. Our results also reveal that the surface-dependent reactivity of these assemblies is a key factor in their catalytic efficiency. Detailed analysis using *operando* SERS and complementary simulations show that distinct orientations of the NRs (horizontal vs. vertical) within the SCs can impact significantly reaction kinetics. Our results underscore the importance of optimizing NR packing and arrangement to maximize plasmonic coupling and, consequently, photocatalytic efficiency. The study also points to the potential challenges and opportunities in improving the accessibility of active sites in these structured assemblies, as the bulk of the SCs is less accessible to reactants due to their dense packing, thus reducing substantially the effective surface area of the heterogeneous catalyst. Overall, this work demonstrates how the design and assembly of 3D plasmonic SCs ~~can open new avenues for highly efficient photocatalysis, offering~~ offer insights into the role of nanostructure orientation and plasmonic coupling in enhancing photocatalytic processes. Future research may focus on further tuning the composition and arrangement of these SCs to explore their potential in a broader range of catalytic applications.

Supporting Information

Supporting Information is available from the Wiley Online Library or from the author.

Acknowledgements

ANR (Agence Nationale de la Recherche) and CGI (Commissariat à l'Investissement d'Avenir) are gratefully acknowledged for their financial support of this work through Labex SEAM (Science and Engineering for Advanced Materials and devices), ANR-10-LABX-0096 and ANR-18-IDEX-0001. Hyperspectral microscopy was supported by the European Research Council (ERC) under European Union's Horizon 2020 Programme (Grant Agreement no. 803220). This work has been sponsored by the Ile-de-France Region in the framework of Respore, the Île-de-France network of Excellence in Porous Solids. The authors acknowledge the ITODYS SEM facility and SOLEIL for the provision of synchrotron radiation facilities (experiments 20231786). We would like to thank Thomas Bizien for assistance in using beamline SWING. This work also was supported by the projects PID2020-118282RA-I00,

RYC2021-033818-I, and FPU21/03137, funded by MCIN/AEI/10.13039/501100011033 and European Union "NextGenerationEU"/PRTR; ED431F 2024/21 funded by Xunta de Galicia; HORIZON-EIC-2022-PATHFINDERCHALLENGES-01-06 (AREMIS, No. 101115149), funded by the European Union Horizon 2020 Research and Innovation Program.

Received: ((will be filled in by the editorial staff))
Revised: ((will be filled in by the editorial staff))
Published online: ((will be filled in by the editorial staff))

4. References

[1] S. Linic, S. Chavez, R. Elias, *Nat. Mater.* **2021**, *20*, 916.

[2] J. Gargiulo, R. Berté, Y. Li, S. A. Maier, E. Cortés, *Acc. Chem. Res.* **2019**, *52*, 2525.

[3] C. Brissaud, L. V. Besteiro, J. Y. Piquemal, M. Comesaña-Hermo, *Sol. RRL* **2023**, *7*, 2300195.

[4] A. Gellé, T. Jin, L. De La Garza, G. D. Price, L. V. Besteiro, A. Moores, *Chem. Rev.* **2020**, *120*, 986.

[5] Y. Zhang, S. He, W. Guo, Y. Hu, J. Huang, J. R. Mulcahy, W. D. Wei, *Chem. Rev.* **2018**, *118*, 2927.

[6] S. Mukherjee, F. Libisch, N. Large, O. Neumann, L. V. Brown, J. Cheng, J. B. Lassiter, E. A. Carter, P. Nordlander, N. J. Halas, *Nano Lett.* **2013**, *13*, 240.

[7] D. F. Swearer, H. Zhao, L. Zhou, C. Zhang, H. Robatjazi, J. M. P. Martirez, C. M. Krauter, S. Yazdi, M. J. McClain, E. Ringe, E. A. Carter, P. Nordlander, N. J. Halas, *Proc. Natl. Acad. Sci.* **2016**, *113*, 8916.

[8] E. Cortés, *Adv. Opt. Mater.* **2017**, *5*, 1700191.

[9] P. K. Jain, W. Qian, M. A. El-Sayed, *J. Am. Chem. Soc.* **2006**, *128*, 2426.

[10] Y. Wy, H. Jung, J. W. Hong, S. W. Han, *Acc. Chem. Res.* **2022**, *55*, 831.

[11] C. Hamon, S. M. Novikov, L. Scarabelli, D. M. Solís, T. Altantzis, S. Bals, J. M. Taboada, F. Obelleiro, L. M. Liz-Marzán, *ACS Photonics* **2015**, *2*, 1482.

[12] D. M. Solís, J. M. Taboada, F. Obelleiro, L. M. Liz-Marzán, F. J. García de Abajo, *ACS Nano* **2014**, *8*, 7559.

[13] M. Herran, S. Juergensen, M. Kessens, D. Hoeing, A. Köppen, A. Sousa-Castillo, W. J. Parak, H. Lange, S. Reich, F. Schulz, E. Cortés, *Nat. Catal.* **2023**, *6*, 1205.

[14] S. K. Boong, C. Chong, J.-K. Lee, Z.-Z. Ang, H. Li, H. K. Lee, *Angew. Chem. Int. Ed.* **2023**, *62*, e202216562.

[15] D. García-Lojo, S. Núñez-Sánchez, S. Gómez-Graña, M. Grzelczak, I. Pastoriza-Santos, J. Pérez-Juste, L. M. Liz-Marzán, *Acc. Chem. Res.* **2019**, *52*, 1855.

[16] G. Bodelón, V. Montes-García, V. López-Puente, E. H. Hill, C. Hamon, M. N. Sanz-Ortiz, S. Rodal-Cedeira, C. Costas, S. Celiksoy, I. Pérez-Juste, L. Scarabelli, A. La Porta, J. Pérez-Juste, I. Pastoriza-Santos, L. M. Liz-Marzán, *Nat. Mater.* **2016**, *15*, 1203.

[17] M. Blanco-Formoso, N. Pazos-Perez, R. A. Alvarez-Puebla, *ACS Omega* **2020**, *5*, 25485.

[18] K. Bian, H. Schunk, D. Ye, A. Hwang, T. S. Luk, R. Li, Z. Wang, H. Fan, *Nat. Commun.* **2018**, *9*, 2365.

[19] S. Sarina, H. Zhu, E. Jaatinen, Q. Xiao, H. Liu, J. Jia, C. Chen, J. Zhao, *J. Am Chem. Soc.* **2013**, *135*, 5793.

[20] E. Peiris, S. Hanauer, T. Le, J. Wang, T. Salavati-fard, P. Brasseur, E. V Formo, B. Wang, P. H. C. Camargo, *Angew. Chemie, Int. Ed.* **2023**, *62*, e202216398.

[21] W. Zhou, Y. Lim, H. Lin, S. Lee, Y. Li, Z. Huang, J. S. Du, B. Lee, S. Wang, A. Sánchez-Iglesias, M. Grzelczak, L. M. Liz-Marzán, S. C. Glotzer, C. A. Mirkin, *Nat. Mater.* **2024**, *23*, 424.

[22] Z. Li, Y. Lim, I. Tanriover, W. Zhou, Y. Li, Y. Zhang, K. Aydin, S. C. Glotzer, C. A. Mirkin, *Sci. Adv.* **2024**, *10*, eadp3756.

[23] J. Marcone, W. Chaâbani, C. Goldmann, M. Impéror-Clerc, D. Constantin, C. Hamon, *Nano Lett.* **2023**, *23*, 1337.

[24] Y. Fan, M. Walls, C. Salzemann, J. M. Noël, F. Kanoufi, A. Courty, J. F. Lemineur, *Adv. Mater.* **2023**, *35*, 2305402.

[25] A. Sánchez-Iglesias, K. Jenkinson, S. Bals, L. M. Liz-Marzán, *J. Phys. Chem. C* **2021**, *125*, 23937.

[26] S. Rodal-Cedeira, V. Montes-García, L. Polavarapu, D. M. Solís, H. Heidari, A. La Porta, M. Angiola, A. Martucci, J. M. Taboada, F. Obelleiro, S. Bals, J. Pérez-Juste, I. Pastoriza-Santos, *Chem. Mater.* **2016**, *28*, 9169.

[27] X. Zhu, H. Jia, X. M. Zhu, S. Cheng, X. Zhuo, F. Qin, Z. Yang, J. Wang, *Adv. Funct. Mater.* **2017**, *27*, 1700016.

[28] Y. Mao, M. E. Cates, H. N. W. Lekkerkerker, *Physica A* **1995**, *222*, 10.

[29] J. Kim, X. Song, F. Ji, B. Luo, N. F. Ice, Q. Liu, Q. Zhang, Q. Chen, *Nano Lett.* **2017**, *17*, 3270.

[30] K. Zhao, T. G. Mason, *Phys. Rev. Lett.* **2007**, *99*, 268301.

[31] K. Zhao, T. G. Mason, *Phys. Rev. Lett.* **2008**, *101*, 148301.

[32] X. Yang, J. Li, Y. Zhao, J. Yang, L. Zhou, Z. Dai, X. Guo, S. Mu, Q. Liu, C. Jiang, M. Sun, J. Wang, W. Liang, *Nanoscale* **2018**, *10*, 142.

[33] S. Gómez-Graña, J. Pérez-Juste, R. A. Alvarez-Puebla, A. Guerrero-Martínez, L. M. Liz-Marzán, *Adv. Opt. Mater.* **2013**, *1*, 477.

[34] R. D. Deegan, O. Bakajin, T. F. Dupont, G. Huber, S. R. Nagel, T. A. Witten, *Nature* **1997**, *389*, 827.

[35] Á. G. Marín, H. Gelderblom, D. Lohse, J. H. Snoeijer, *Phys. Rev. Lett.* **2011**, *107*, 85502.

[36] H. Hu, R. G. Larson, *J. Phys. Chem. B* **2006**, *110*, 7090.

[37] C. Hamon, C. Goldmann, D. Constantin, *Nanoscale* **2018**, *10*, 18362.

[38] Y. F. Huang, M. Zhang, L. Bin Zhao, J. M. Feng, D. Y. Wu, B. Ren, Z. Q. Tian, *Angew. Chem. Int. Ed.* **2014**, *53*, 2353.

[39] I. Sapurina, J. Stejskal, *Polym. Int.* **2008**, *57*, 1295.

[40] H. D. Tran, J. M. D'Arcy, Y. Wang, P. J. Beltramo, V. A. Strong, R. B. Kaner, *J. Mater. Chem.* **2011**, *21*, 3534.

[41] Y. Lu, S. H. Lam, W. Lu, L. Shao, T. H. Chow, J. Wang, *Nano Lett.* **2022**, *22*, 1406.

[42] Y. Negrín-Montecelo, C. Brissaud, J. Y. Piquemal, A. O. Govorov, M. A. Correa-Duarte, L. V. Besteiro, M. Comesaña-Hermo, *Nanoscale* **2022**, *14*, 11612.

[43] E. Cortés, W. Xie, J. Cambiasso, A. S. Jermyn, R. Sundararaman, P. Narang, S. Schlücker, S. A. Maier, *Nat. Commun.* **2017**, *8*, 14880.

[44] A. G. M. da Silva, T. S. Rodrigues, V. G. Correia, T. V. Alves, R. S. Alves, R. A. Ando, F. R. Ornellas, J. Wang, L. H. Andrade, P. H. C. Camargo, *Angew. Chem. Int. Ed.* **2016**, *55*, 7111.

[45] B. Qiu, Z. Li, X. Wang, X. Li, J. Zhang, *J. Polym. Sci. Part A Polym. Chem.* **2017**, *55*, 3357.

[46] J. P. Pouget, M. E. Józefowicz, A. J. Epstein, X. Tang, A. G. MacDiarmid, *Macromolecules* **1991**, *24*, 779.

[47] Y. Jiang, S. Li, S. Wang, Y. Zhang, C. Long, J. Xie, X. Fan, W. Zhao, P. Xu, Y. Fan, C. Cui, Z. Tang, *J. Am. Chem. Soc.* **2023**, *145*, 2698.

[48] Y. Jiang, W. Zhao, S. Li, S. Wang, Y. Fan, F. Wang, X. Qiu, Y. Zhu, Y. Zhang, C. Long, Z. Tang, *J. Am. Chem. Soc.* **2022**, *144*, 15977.

[49] J. K. Stille, *Angew. Chemie Int. Ed.* **1986**, *25*, 508.

[50] C. Cordovilla, C. Bartolomé, J. M. Martínez-Ilarduya, P. Espinet, *ACS Catal.* **2015**, *5*, 3040.

[51] H. Shoukat, A. A. Altaf, M. Hamayun, S. Ullah, S. Kausar, M. Hamza, S. Muhammad, A. Badshah, N. Rasool, M. Imran, *ACS Omega* **2021**, *6*, 19606.

[52] S. Jiao, K. Dai, L. V. Besteiro, H. Gao, X. Chen, W. Wang, Y. Zhang, C. Liu, I. Pérez-Juste, J. Pérez-Juste, I. Pastoriza-Santos, G. Zheng, *ACS Catal.* **2024**, *14*, 6799.

[53] D. Wang, F. Shi, J. Jose, Y. Hu, C. Zhang, A. Zhu, R. Grzeschik, S. Schlücker, W. Xie, *J. Am. Chem. Soc.* **2022**, *144*, 5003.

[54] Y. Zhao, L. Du, H. Li, W. Xie, J. Chen, *J. Phys. Chem. Lett.* **2019**, *10*, 1286.

[55] E. D. Emmons, J. A. Guicheteau, A. W. Fountain, A. Tripathi, *Phys. Chem. Chem. Phys.* **2020**, *22*, 15953.

[56] P. Jiang, Y. Dong, L. Yang, Y. Zhao, W. Xie, *J. Phys. Chem. C* **2019**, *123*, 16741.

[57] Y.-F. Huang, H.-P. Zhu, G.-K. Liu, D.-Y. Wu, B. Ren, Z.-Q. Tian, *J. Am. Chem. Soc.* **2010**, *132*, 9244.

[58] L. V. Besteiro, X. T. Kong, Z. Wang, G. Hartland, A. O. Govorov, *ACS Photonics* **2017**, *4*, 2759.

[59] E. Y. Santiago, L. V. Besteiro, X. T. Kong, M. A. Correa-Duarte, Z. Wang, A. O. Govorov, *ACS Photonics* **2020**, *7*, 2807.

[60] Y. Kang, S. M. João, R. Lin, K. Liu, L. Zhu, J. Fu, W.-C. (Max) Cheong, S. Lee, K. Frank, B. Nickel, M. Liu, J. Lischner, E. Cortés, *Nat. Commun.* **2024**, *15*, 3923.

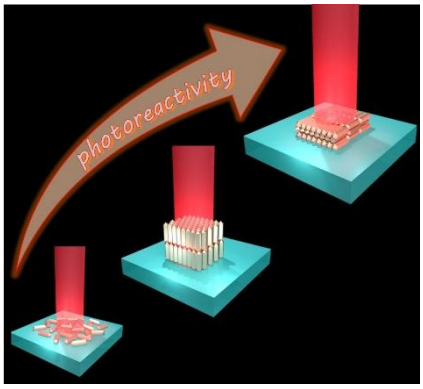
Photoreactivity

Faceted 3D Supercrystals for Plasmonic Photocatalysis: Design, Reactivity and Operando Studies

Charlène Brissaud, Wajdi Chaâbani, Jesús Giráldez-Martínez, Meyssa Mockbel, Eva Yazmin Santiago, Jaime Gabriel Trazo, Rahul Nag, Stéphanie Lau-Truong, Gaëlle Blond, Marco Faustini, Cyrille Hamon, Lucas V. Besteiro, Jean-Yves Piquemal, Miguel Comesaña-Hermo**

Charlène Brissaud, Wajdi Chaâbani, Meyssa Mockbel, Rahul Nag, Stéphanie Lau-Truong, Jean-Yves Piquemal, Miguel Comesaña-Hermo
Université Paris Cité, CNRS, ITODYS, 75006 Paris (France)
E-mail: charlene.brissaud@gmail.com, miguel.comesana-hermo@u-paris.fr

Jesús Giráldez-Martínez, Eva Yazmin Santiago, Lucas V. Besteiro
CINBIO, Universidade de Vigo, Department of Physical Chemistry, 36310 Vigo (Spain)

Jaime Gabriel Trazo, Cyrille Hamon
Université Paris-Saclay, CNRS, Laboratoire de Physique des Solides, 91405 Orsay (France)

Gaëlle Blond
Université de Strasbourg, CNRS, Laboratoire d'Innovation Thérapeutique, 67000 Strasbourg (France)

Marco Faustini
Sorbonne Université, CNRS, UMR 7574, Chimie de la Matière Condensée de Paris,75005 Paris (France)

Marco Faustini
Institut Universitaire de France (IUF), 75231 Paris (France)

1. Chemicals

Aniline 99% ($C_6H_5NH_2$), bromobenzene ≥ 99% (C_6H_5Br, BB), 4-bromothiophenol 95% (BrC_6H_4SH, 4-BTP), cetyltrimethylammonium bromide ≥ 96.0% ($CH_3(CH_2)_{15}N(Br)(CH_3)_3$, CTAB), cetyltrimethylammonium chloride solution 25 wt.% ($CH_3(CH_2)_{15}N(Cl)(CH_3)_3$, CTAC), citric acid 99% ($HOC(COOH)(CH_2COOH)_2$), dimethyl sulfoxide ($(C2H_3)_2SO$, DMSO), hydrochloric acid 37 wt.% (HCl), L-ascorbic acid ($C_6H_8O_6$, AA), m-tolylboronic acid 97% ($(CH_3)C_6H_4B(OH)_2$), m-TBA), palladium(II) chloride 99% ($PdCl_2$), sodium borohydride ($NaBH_4$), tetrachloroauric acid ($HAuCl_4 \cdot 3H_2O$) and tributyl(vinyl)tin 97% ($(C_4H_9)_3Sn(C_2H_4)$, TBVT) were purchased from Sigma-Aldrich. Toluene ($C_6H_5CH_3$) and cyclohexane (C_6H_{12}) were purchased from Carlo Erba. Milli-Q water (resistivity 18.2 MΩ.cm at 25 °C) was used in all syntheses.

2. Materials and methods

a. Synthesis of the plasmonic building blocks

Seeds. Citrate-capped pentatwinned (PTW) seeds were synthesized using a procedure reported by Sánchez-Iglesias and coworkers with some modifications.[1,2] Initially, $HAuCl_4$ (100 µL, 25 mM) was added to a 10 mL aqueous solution containing 5 mM of citric acid and 50 mM of CTAC. The mixture was vigorously stirred at room temperature to form a vortex in the center of which $NaBH_4$ (250 µL, 25 mM) was introduced. After 2 min of vigorous stirring, the mixture was placed in a water bath at 90 °C for 2 h under gentle magnetic stirring.

PTW Au NRs. The NRs were synthesized using the procedure described by Sánchez-Iglesias and coworkers.[2] An initial aqueous solution of 500 mL containing CTAB (375 mg) and CTAC (66.1 mL, 0.76 M) was prepared and carefully sonicated until complete dissolution of the former. Subsequently, $HAuCl_4$ (2.5 mL, 25 mM) was introduced in the binary surfactant mixture. The solution was sonicated and then left undisturbed at a given temperature for 30 min. Afterwards, the reducing agent, AA (976 µL, 0.1 M, AA/Au^{3+} molar ratio of 1.5), was quickly injected in the mixture which was then vigorously shaken by hand. Finally, the seeds were rapidly introduced (Au^{3+}/Au^0 molar ratio of 133) and the solution was immediately thoroughly shaken again for 30 s. Then, the growth solution was left undisturbed for 1 h in a thermostated water bath at the same temperature than the one used for the thermalization of the $HAuCl_4$/CTAB/CTAC mixture. At the end of the reaction, the NPs were centrifuged (8000 rpm, 30 min) and redispersed in 0.1 M CTAC. This process was repeated two more times. Given that

PTW Au NRs were accompanied by an undesired population of more isotropic NPs (spheres and octahedra), purification was performed by flocculation. Typically, the washed NPs were concentrated in a small volume (< 2 mL) of CTAC 0.12 M in a glass test tube that was left undisturbed overnight. After this, PTW Au NRs precipitated at the bottom of the tube while the smaller and more isotropic NPs remained in solution and could be removed. The precipitate was then redispersed in 0.1 M CTAC. The dimensions obtained from TEM were 100.8 ± 6.6 nm of length and 22.8 ± 1.2 nm of width (aspect ratio: 4.4). To obtain PTW Au NRs with a longitudinal plasmon band centered at ca. 800 nm, we performed the growth at 20 °C.

Synthesis of Au@Pd NRs. The core-shell NRs were synthesized using a seed-mediated growth method adapted from the literature and consisting in the reduction of a palladium salt onto PTW Au NRs used as seeds.[3] Prior to the experiment, a 5 mM H_2PdCl_4 solution was prepared by dissolution of $PdCl_2$ (8.87 mg) in an aqueous solution of HCl (10 mL, 10 mM). Typically, a given amount of PTW Au NRs (longitudinal plasmon band centered at ca. 800 nm) previously washed and redispersed in 10.8 mM CTAB was introduced in an aqueous solution of CTAB (10.8 mM) in order to obtain a final concentration of $5 \cdot 10^{-5}$ M in 3 mL. Subsequently, H_2PdCl_4 (19.5 µL, 5 mM) was added under sonication. Then, HCl (55.7 µL, 0.1 M) was injected under sonication to adjust the pH of the growth solution to ca. 5, followed by the addition of AA (139 µL, 40 mM). The solution was left undisturbed in a water bath at 60 °C for 1 h. The Au@Pd NRs were then washed by centrifugation-redispersion cycles (8000 rpm, 30 min, 3 times) and redispersed in 2.5 mM CTAC or CTAB. After confirming with TEM that the Pd shell was homogeneous and thin enough, the synthesis was scaled-up to produce a sufficient amount of Au@Pd NRs for the self-assembly process. The dimensions of the Au@Pd NRs were of 118.2 ± 5.1 nm in length and 27.0 ± 1.0 in width (aspect ratio: 4.4).

b. Self-assembly of PTW Au and Au@Pd NRs

In a typical procedure, PTW Au NRs and Au@Pd NRs were washed several times in 2.5 mM CTAC or CTAB and then the solutions were concentrated to obtain a final metal concentration of 16 mM. Prior to the deposition, the substrates were washed with aqua regia and rinsed in water, EtOH and then acetone (10 min under sonication for each cycle). The substrates were then dried in an oven and cleaned under oxygen plasma (0.3 mbar, 30 s). Then, 10 µL of the NRs solution were drop-casted, either on a silicon wafer or a glass slide, which was then introduced in a Petri dish in the presence of water droplets. The solutions were left undisturbed until complete drying (several days). The presence of water in the Petri dish permitted to slow

down the evaporation process and to form well-organized PTW Au and Au@Pd NRs SCs. Before any photocatalytic experiments, organic molecules were removed from the Au and Au@Pd SC surfaces by oxygen plasma cleaning (0.3 mbar, 30 s) and soaking in EtOH (10–20 seconds).

c. Theoretical methods

The commercial software package COMSOL Multiphysics, based on the Finite Element Method (FEM), was used to solve Maxwell´s equations in order to obtain the optical and electrodynamic response of the metallic NPs. The 3D geometries of the Au and Au@Pd NRs used in the models were created following TEM images and statistical data of their sizes from the experimental samples. The modelled Au NRs are 100.5 nm long and 22.5 nm wide; and the pentagonal-shaped Au@Pd NRs are 117.2 nm long and have a vertex to side width of 26.9 nm and vertex to vertex size of 17.1 nm. The permittivity of the objects was modelled using the experimental bulk permittivity of Au[4] and Pd.[5] The boundary between the two metals in the bimetallic Au@Pd NRs was considered sharp, i.e. no alloy gradient was modelled. The hexagonal pattern found in the SEM images of the SCs was replicated in the models by designing a unit cell and implementing periodic boundary conditions (PBC). These periodic SCs were immersed in a dielectric medium of permittivity $\varepsilon = 1$ (air). The spectra in the manuscript show the average response of two orthogonal polarizations (aligned or orthogonal to the longitudinal axis of the rod, if in horizontal arrangement; a single polarization if in vertical), to account for the average among relative orientations between laser and SC in the experiment. Depending on the relative disposition of the NRs (parallel or perpendicular with respect to the substrate), the periodic COMSOL models were created with different number of rods per unit cell. In the case of parallel or horizontal disposition, the unit cell contains 8 NRs and they are distributed in 5 layers (Figure 5e in the manuscript). When considering the perpendicular or vertical arrangement, the unit cell contains 4 NRs, 2 per layer (Figure 5e in the manuscript). Both unit cells include these numbers of NRs to account for the NR positions in a close-packed arrangement. The interparticle distance between adjacent NRs in all the models is 2.5 nm.

Hot carrier excitation rates ($Rate_{HE}$) were computed using a semi-classical formalism which models the optical transitions of electrons that can occur in a metal due to the loss of translational symmetry arising from collisions of the excited electrons with the boundaries of

the object. A detailed description of this formalism can be found in previous publications.[6,7] Numerically:

$$Rate_{\mathrm{HE}}(\omega) = \int_S \frac{2}{\pi^2}\frac{e^2 E_{\mathrm{F}}^2}{\hbar}\frac{1}{(\hbar\omega)^3}\left|E_{\mathrm{normal}}(\mathbf{r},\omega)\right|^2 \mathrm{ds}$$

where $E_{normal}(r, \omega)$ is the component of the electric field normal to the NP´s outer surface, measured immediately inside the metal; E_F is the Fermi energy of the metal at the outer surface; $\hbar\omega$ is the energy of the incoming photon; and S is the outer surface of the NP. To be able to compare the $Rate_{HE}$ of different periodic models, we normalized the computed rates by the area of the horizontal section of the unit cell (A_{cell}) used in each periodic model ($Rate_{HE}$ / A_{cell} [$1/(nm^2 \bullet s)$]).

The spectra of $Rate_{HE}$ obtained by integrating over all the external surfaces of the NRs forming the SCs, independent of depth, is shown in Figure S11. In an hypothetical scenario in which all the deep structure of the SC would contribute to the photocatalysis, using the vertical arrangement would be advantageous. Nevertheless, the reactions are expected to take place in the top layer of the SCs. For this reason, we computed the $Rate_{HE}$ integrating the surface of the top layer of the multilayer models, and for different highs (values of the z-coordinate). We repeated this integration to analyze the dependence of the $Rate_{HE}$ / A_{cell} at the SERS wavelength (633 nm) on the range of values taken for the z-coordinate (Figure 5e).

The field enhancement (FE) achieved by the metal NPs in the two different dispositions was quantified using the following expression:

$$FE = \left|\mathbf{E}(\mathbf{r})\right|^2 / E_0^2$$

where E(r) is the electric field at point r, and E_0 is the amplitude of the electric field of the incoming planewave (Figure S12-S13).

The excess temperature results shown in Figure S18 were obtained by solving the heat transfer equation in systems with the same periodicity as the rest of computational models. The model systems are irradiated by a moderate light intensity of I_0 = 130 W/cm^2, and averaging two orthogonal linear polarizations. The heat source in the cell are the dissipation losses due to absorption in the metal nanorods, and the only heat sink present are the top and bottom boundary conditions, which are set at room temperature and placed at position suitably far (ca. 1500 nm) from both top and bottom faces of the SC to avoid clamping the maximum temperature increase.

The metal NRs are surrounded by air, as in the previously discussed models, and neither convection nor radiative cooling are modelled, so that the temperature increases found in the simulations can be considered conservative overestimates of the maximum temperature obtained under the chosen light intensity, especially when we are modelling infinite 2D systems. The average excess temperatures reported next to each system in Figure S18 were obtained by averaging this magnitude over the same surfaces used in Figure 5, considered to be the available catalytic surfaces. However, it is clear from the color maps that the temperature at the metal is homogeneous, as one expects from materials with large thermal conductivity.

d. Photocatalytic studies

The SCs (Au or Au@Pd depending on the chemical reaction under study) deposited on a glass slide were placed in the reaction medium after homogenization under magnetic stirring. We consider [Au] = 16 mM for both Au and Au@Pd SCs. Photocatalytic experiments were conducted in a quartz cuvette (1 cm optical path) under magnetic stirring. The irradiation source was a LOT solar simulator (300 W Xe lamp, λ = 350–2400 nm) equipped with an optical fiber (output power density: 50 mW/cm^2). Standard spectra of the lamp can be obtained from Quantum Design (www.qd-europe.com). In order to ensure a good control of the irradiation conditions and the temperature of the photocatalytic cell, the experiments were performed inside a cuvette holder (QPOD-3) from Quantum Northwest (USA) that allows the control and monitoring of the macroscopic temperature.

Oxidation of aniline. 2 μmol of aniline were added to 2 mL of DMSO in a 4 mL quartz cuvette. The reaction was performed at 25 °C, under irradiation and magnetic stirring for 72 h, in the presence of Au SCs as photocatalysts. When needed, the experiment was conducted while bubbling O_2 in the solution. The reaction products were analyzed by absorption spectroscopy, GC-MS and HRTEM. Control experiments were carried out using PTW Au NRs (same amount) randomly deposited on a glass slide. When needed, a certain amount of TEMPO (final concentration: 0.93 mM) is included in the reaction mixture.

Stille cross-coupling reaction. BB (0.01 mmol) and tributyl(vinyl)tin (TVBT, 0.01 mmol) were mixed in 3 mL of toluene in the presence of Au@Pd SCs. The mixture was irradiated for 24 h at 90 °C under magnetic stirring. The reaction products were analyzed and quantified by GC-MS. Control experiments were performed using Au@Pd NRs (same amount) randomly

deposited on a glass slide. When needed, a certain amount of TEMPO (final concentration: 5 mM) is included in the reaction mixture.

Macroscopic thermal evaluation under photocatalytic conditions. Au and Au@Pd SCs deposited on a glass slide were introduced in a quartz cuvette (1 cm optical path length) under magnetic stirring in the solvents used for the photocatalytic studies: DMSO and toluene, respectively. In both cases, a thermostated oil bath was used to ensure uniform temperature distribution in the solution. Surface temperature measurements of the SCs were performed with a FLIR EX Series IR camera, both under dark conditions and during irradiation with a solar simulator (output power density: 50 mW/cm^2). In the irradiated experiments, a stabilization period of 5 minutes was allowed after switching on the light source before measurements were taken. Under these conditions, no significant macroscopic temperature increase was detected.

Sample and solvent	T of the oil bath	T without irradiation	T with irradiation
Au SCs in DMSO	25.0 °C	**25.4 °C**	**25.4 °C**
Au@Pd SCs in toluene	90.0 °C	**85.0 °C**	**85.3 °C**

Operando SERS reactivity. SERS spectra were recorded using a LabRAM HR Evolution Nano spectrometer (600 line mm^{-1}).

Au@Pd SCs: experiments were conducted at room temperature using a 633 nm He-Ne laser source (100x objective, 0.76 mW output power). Prior to the experiment, an EtOH solution of 4-bromobenzenethiol (4-BTP, 10^{-4} M) was deposited on the Au@Pd SCs. 4-BTP was chosen instead of BB to ensure a correct adsorption of the molecules onto the metal surface. The excess of 4-BTP was removed after drying by plunging the SCs into an EtOH bath and a second solution of m-TBA (10^{-4} M) in EtOH was subsequently deposited. The excess of m-TBA was also removed by EtOH rinsing. The reaction kinetics were followed by measuring the intensity ratio between the 1580–1600 cm^{-1} and 1556 cm^{-1} peaks over time (referred to as $I_{product}$ / $I_{reactant}$). In Figure 5d, we consider that at t=0 the ratio $I_{product}$ / $I_{reactant}$ = 0. Nevertheless, this cannot be established experimentally since the first SERS spectrum recorded already implies the irradiation of the substrate for 20 s.

Au SCs: experiments were conducted at room temperature using a 633 nm He-Ne laser source (100x objective, 0.25 mW output power). Prior to the experiment, an EtOH solution of 4-

aminothiophenol (4-ATP, 10^{-5} M) was deposited on the Au SCs. The reaction kinetics towards the formation of dimercaptoazobenzene (DMAB) were followed by measuring the intensity ratio between the 1436 cm^{-1} and 1070 cm^{-1} peaks over time (referred to as $I_{product}$ / $I_{reactant}$).[8] In Figure S13, we consider that at t=0 the ratio $I_{product}$ / $I_{reactant}$ = 0. Nevertheless, this cannot be established experimentally since the first SERS spectrum recorded already implies the irradiation of the substrate for 0.5 s.

3. Characterization techniques

a. UV-visible-NIR spectroscopy

UV-visible-NIR absorbance spectra were collected with a Perkin Elmer Lambda 1050 spectrophotometer (λ = 200–2500 nm) using quartz cuvettes with a 0.5 cm optical path length.

b. Electron microscopies

SEM images were obtained using a ZEISS Gemini SEM 360 instrument equipped with an Oxford Instruments Ultim Max 170 mm^2 detector and working at an acceleration voltage of 5 kV. TEM and HRTEM images were obtained using a JEOL 2100+ transmission electron microscope operating at an acceleration voltage of 200 kV.

c. Small-angle X-ray scattering (SAXS)

SAXS was performed at the SWING beamline of the SOLEIL synchrotron (Saint-Aubin, France), at a beam energy of 16 keV with a sample-to-detector distance of 6.14 m. The beam size was approximately 500 µm × 200 µm (horizontal x vertical). All measurements were done at room temperature (295 K). To obtain NP form factor data, dilute aqueous NP suspensions were put in round borosilicate glass capillaries with diameter d = 1.6 mm, which were then placed standing upright in sample holders. To obtain SC structural data on the drop-casted samples on glass slides, the slides were placed on sample holders such that the incident X-ray beam was perpendicular to the plane of the glass. For each sample, a series of points were measured along a radial line of the sample droplet, starting from the glass outside the droplet, then at the droplet edge, then at the center of the droplet and finally some distance past the center. Data treatment was done using the Foxtrot software developed at the beamline (https://www.synchrotron-soleil.fr/fr/lignes-de-lumiere/swing).

d. Hyperspectral microscopy

Hyperspectral imaging was used to characterize the optical properties of the assemblies at the single SC level. This analysis was performed with a hyperspectral microscope (Cytoviva) via a push-broom method with an acquisition time of 1 s per line. Hyperspectral images provide a spectral map of the backward scattering of the plasmonic SC. The acquisitions were made in dark field mode using either x10 or x100 dark-field objectives (reflection mode).

e. Gas chromatography coupled to mass spectrometry (GC-MS)

Reaction products from photocatalytic transformations were analyzed by a GCMS-QP 2010 SE Shimadzu gas chromatograph-mass spectrometer equipped with an AOC-20i auto-injector and a SH-Rxi-5ms capillary column (0.25 mm, length: 30 m, 5% diphenyl/95% dimethylpolysiloxane). The main parameters used for the GC-MS analysis are reported in the tables below.

	Column oven temperature (°C)	Injection temperature (°C)	Injection mode
Injection conditions	50	250	Split (split ratio 100)

	Flow control mode	Pressure (kPa)	Total flow (mL min^{-1})	Column flow (mL min^{-1})	Purge flow (mL min^{-1})
Carrier gas conditions	Linear velocity (42.9 cm s^{-1})	81.8	144.4	1.4	3.0

	Initial temperature (°C)	Final temperature (°C)	Ramping rate (°C min^{-1})
Column conditions	50	250	10

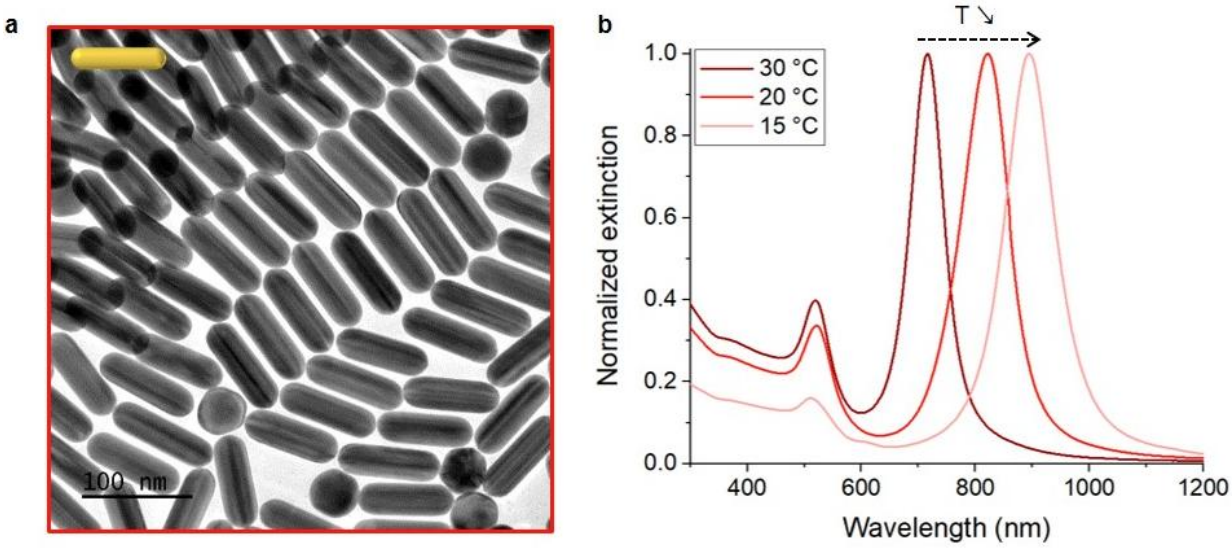

Figure S1. Characterization of the Au NRs. **a)** TEM image of PTW Au NRs. b**)** Normalized extinction spectra of PTW Au NRs synthesized at different temperatures showing that the aspect ratio increases as the temperature of the growth step decreases. In the present work, we have chosen Au NRs synthesized at 20 °C.

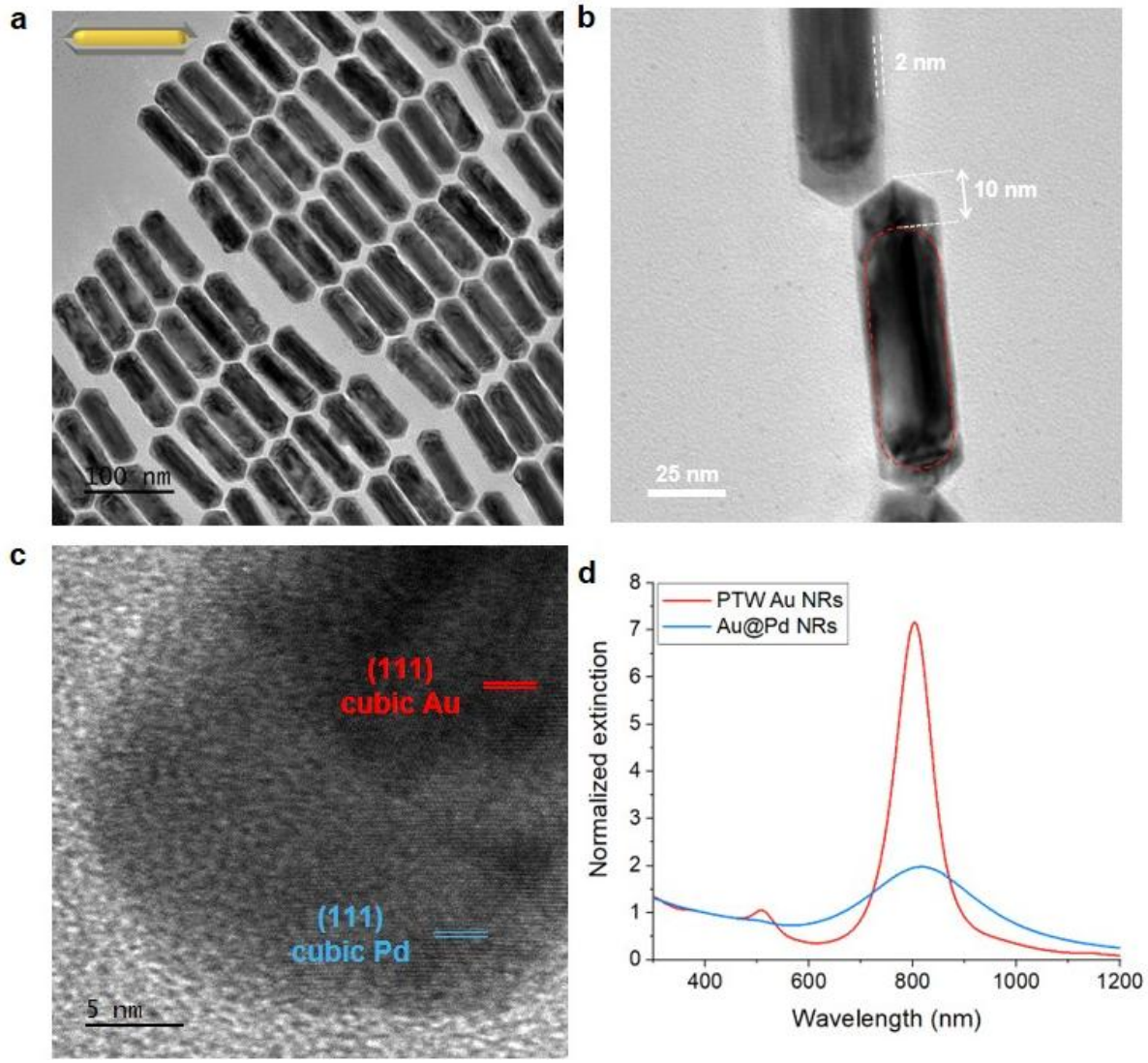

Figure S2. Characterization of the Au@Pd NRs. a, b) TEM and c) HRTEM images of the Au@Pd NRs. d) Normalized extinction spectra of the NRs before (red) and after (blue) deposition of Pd.

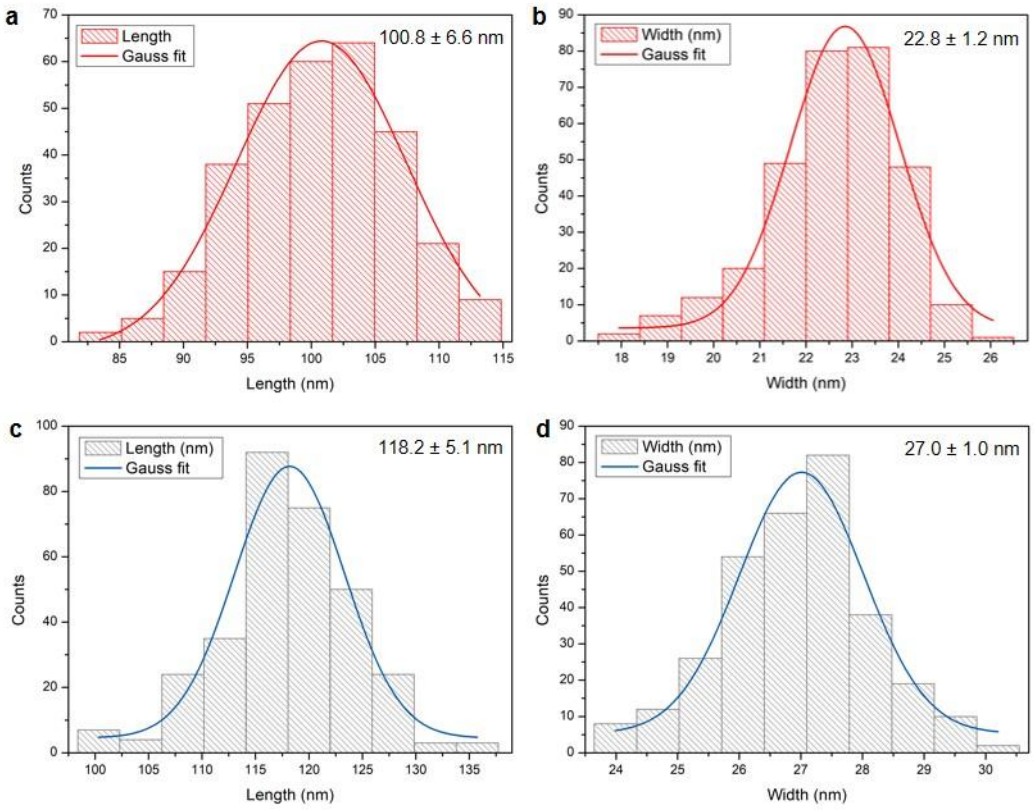

Figure S3. Histograms of the size distribution of a, b) Au NRs and c, d) Au@Pd NRs.

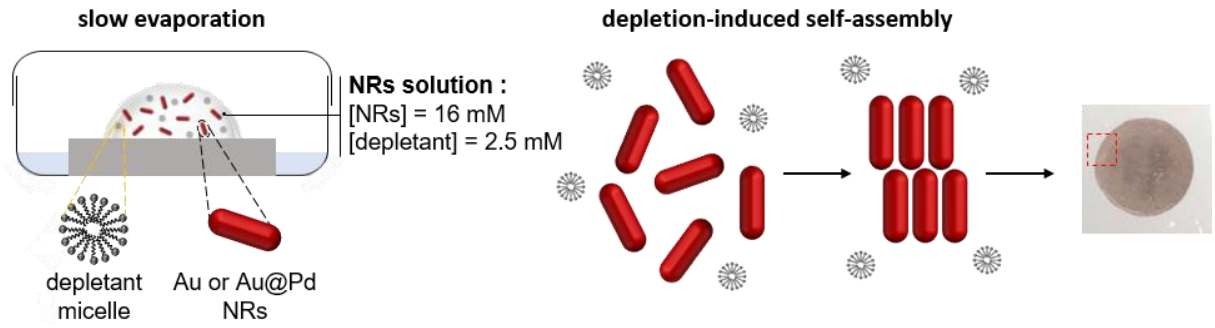

Figure S4. Schematic representation of the evaporation- and depletion-induced formation of SCs together with a photograph of the resulting deposit on a glass slide. Adapted from [9].

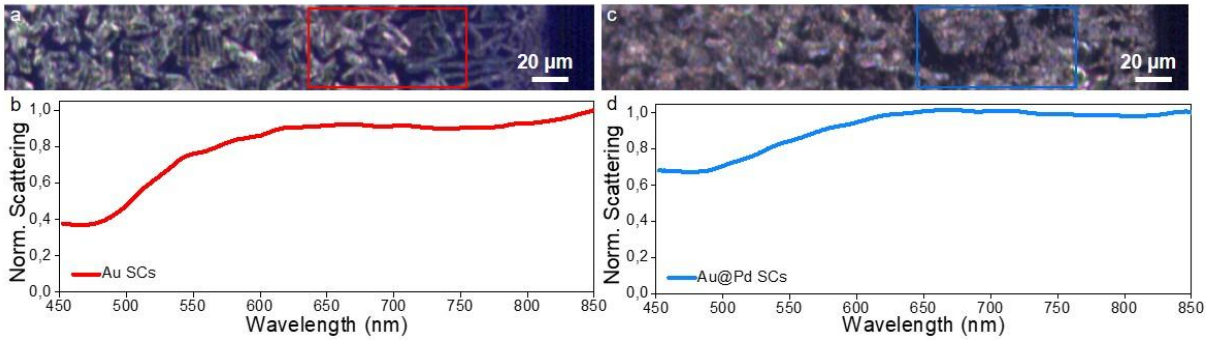

Figure S5. Hyperspectral images (top) and corresponding scattering spectra (bottom) of a given area of glass supports containing the Au (a, b) and Au@Pd (c, d) SCs, respectively. The selected regions used to record the spectra are highlighted in the images and correspond to the integration of 100x50 pixels and an area of 3775 μm^2.

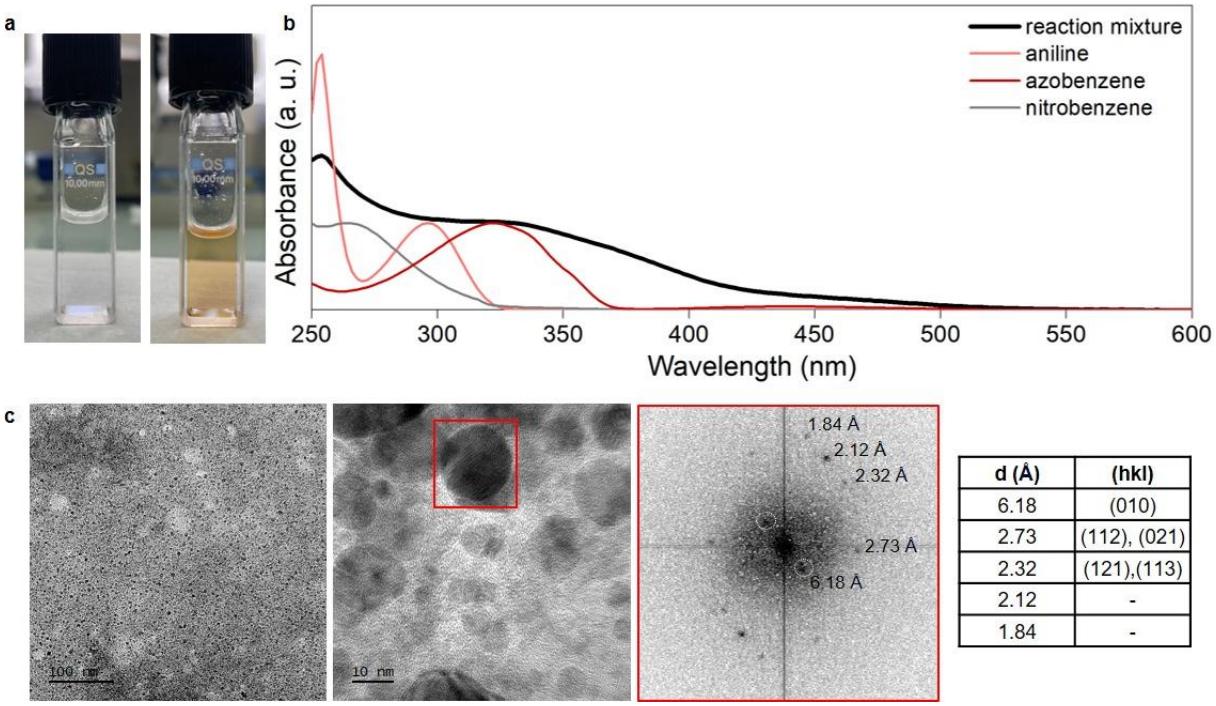

d (Å)	(hkl)
6.18	(010)
2.73	(112), (021)
2.32	(121),(113)
2.12	-
1.84	-

Figure S6. a) Photographs of the reaction medium before (left) and after (right) irradiation in the presence of Au SC photocatalysts. b) UV-visible spectra of the reaction medium, aniline and different possible products recorded in DMSO. c) TEM and HRTEM images of the reaction product, together with the corresponding FT. The table on the right shows the atomic distances measured which correspond to those of pseudo-orthorhombic PANI.[10]

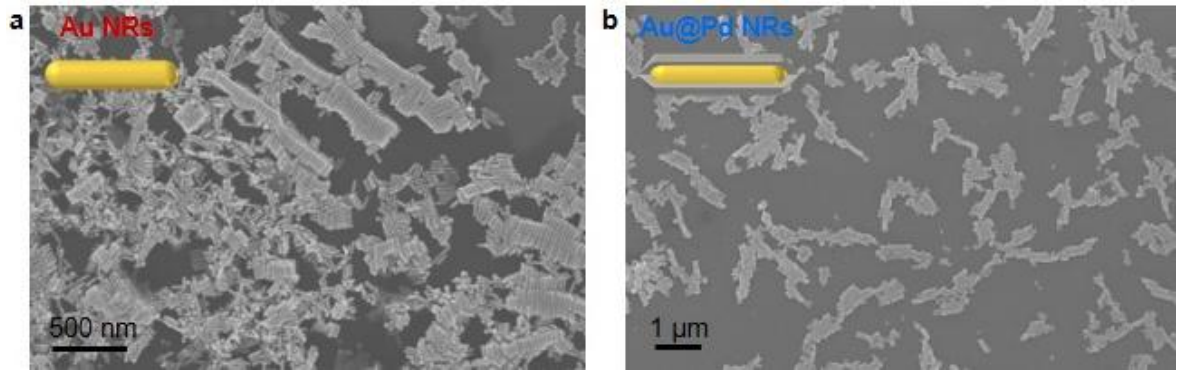

Figure S7. SEM images of random deposits of a) Au and b) Au@Pd NRs onto silicium substrates.

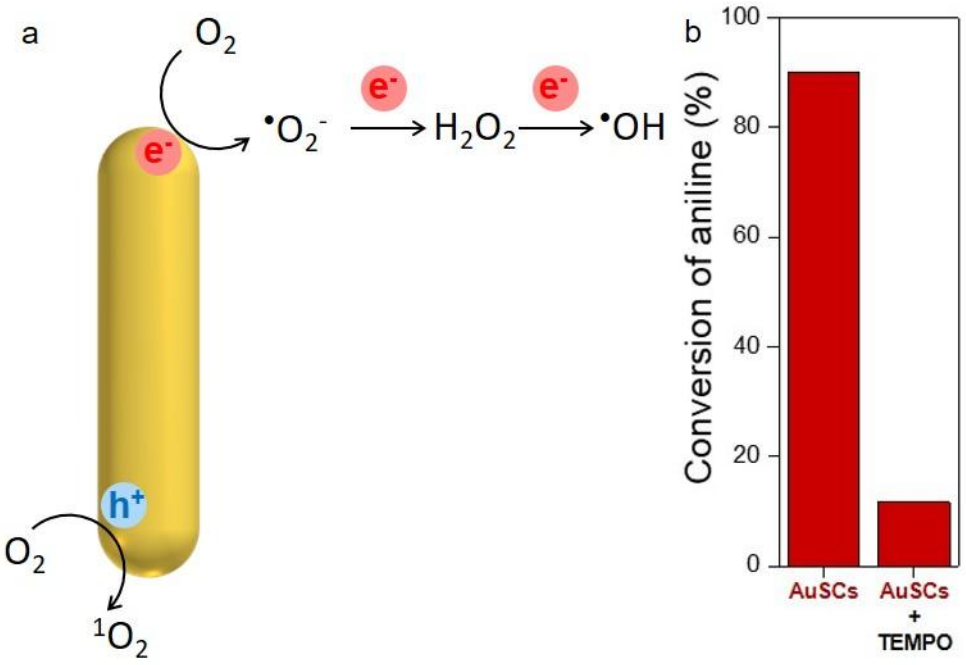

Figure S8. (a) Schematic representation of the cascade of ROS produced upon plasmonic excitation and in the presence of O_2.[11] (b) Photocatalytic transformation of aniline in the presence of the Au SCs under normal reaction conditions and in the presence of a ROS scavenger.

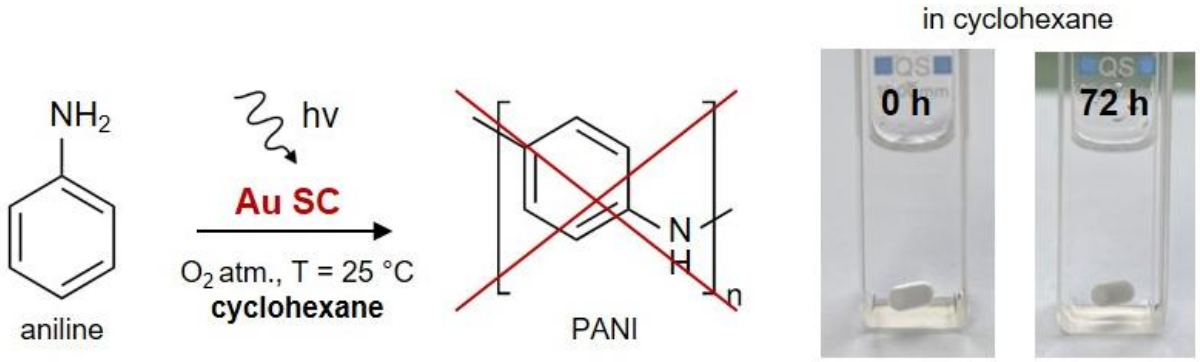

Figure S9. Reaction conditions of the control experiment for aniline photo-oxidation in cyclohexane. The reaction medium remains colorless after 72 hours of irradiation in the presence of the photocatalyst. GC-MS demonstrates that aniline concentration remains constant and no product was observed by TEM or absorption spectroscopy. The same result has been obtained in ethanol.

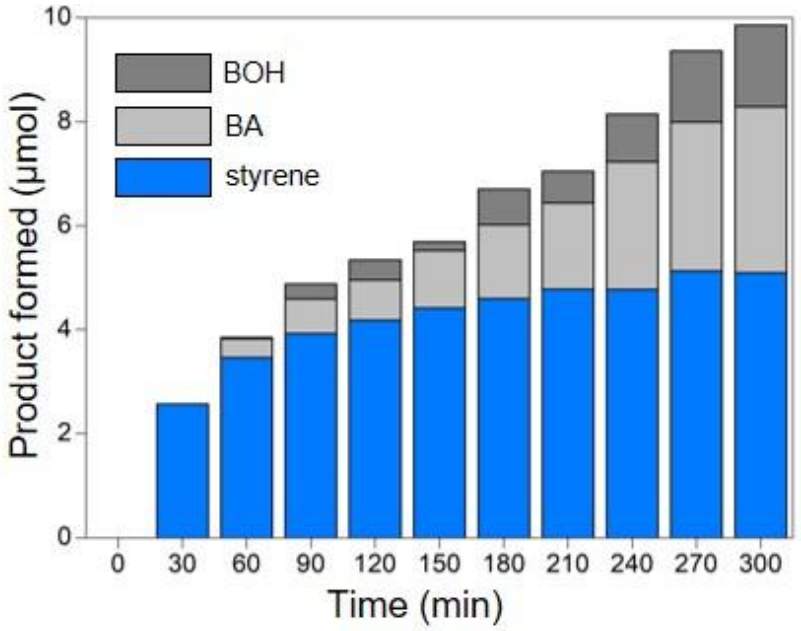

Figure S10. Kinetic study of the Stille reaction under standard conditions in order to follow the relative amount of the three different products formed.

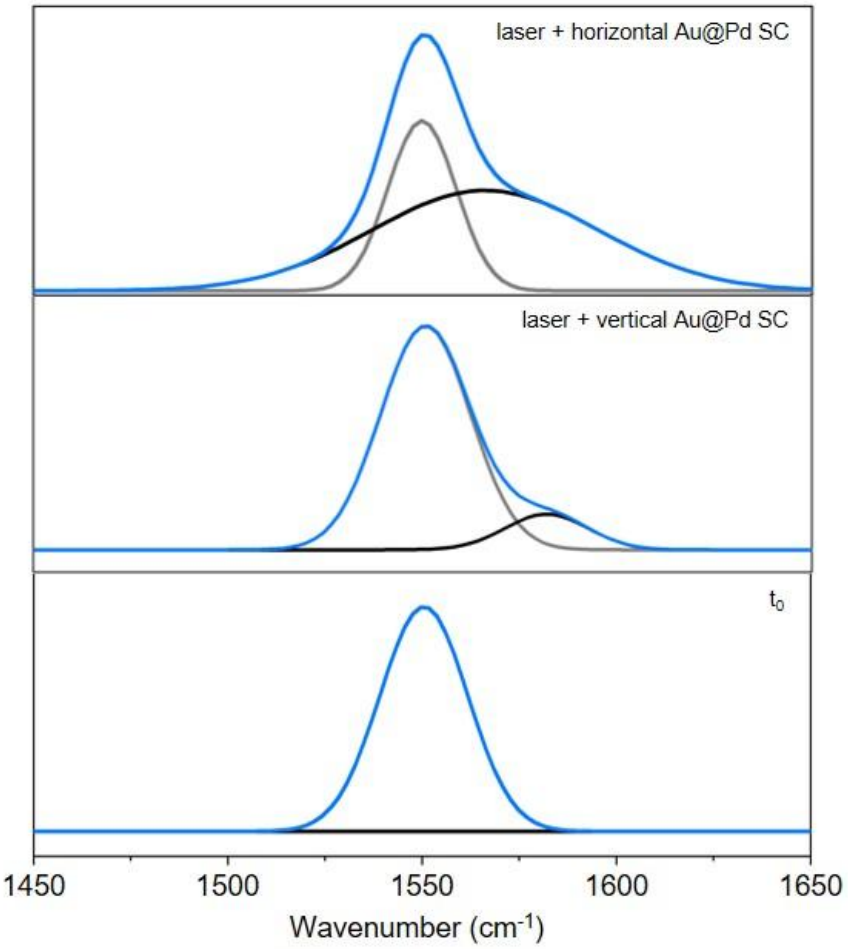

Figure S11. Relative contributions of 4-BTP (gray) and the cross-coupling product (black) at different reaction times obtained from the C–C cross-coupling reactivity on the Au@Pd SCs monitored in *operando* conditions. These fitted curves obtained from the deconvoluted SERS spectra are used to quantify the reaction kinetics after background subtraction.

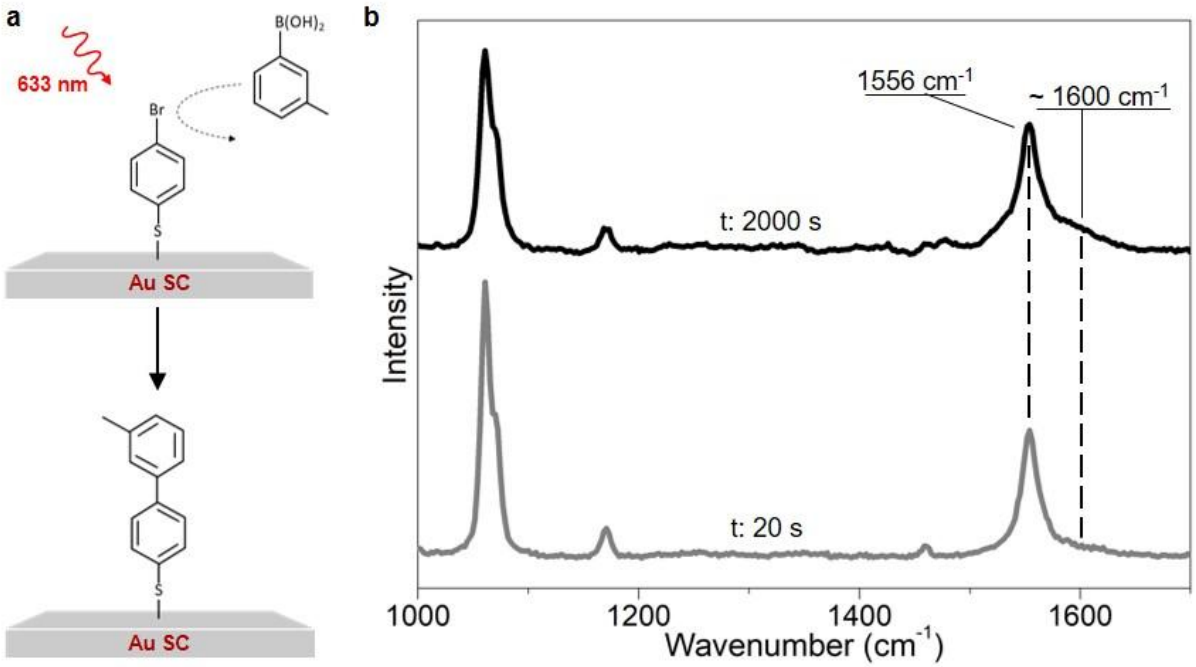

Figure S12. Monitoring of C–C cross-coupling via *operando* SERS on Au SCs. a) Schematic representation of the reaction at the surface of an Au SC. b) Raman spectra recorded on a horizontal Au SC at different irradiation times. Irradiation conditions: λ_{exc}: 633 nm, 100x obj., 0.76 mW power + 20 s acquisition time.

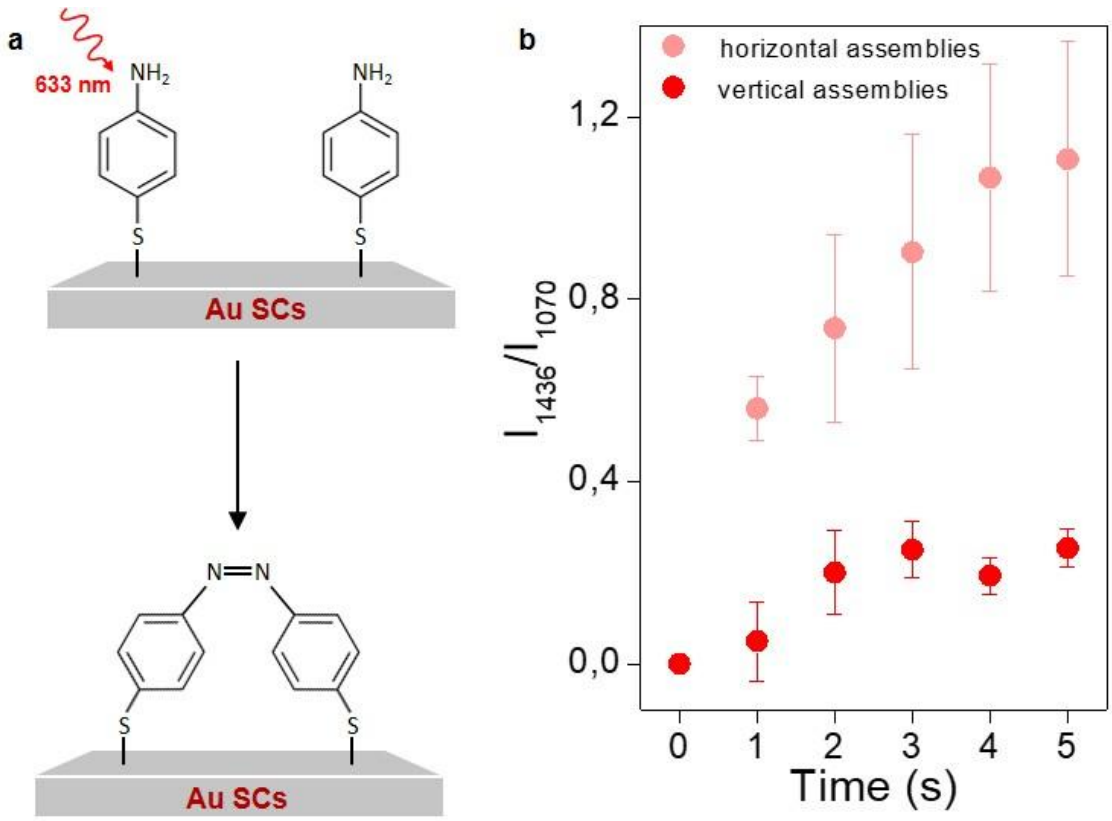

Figure S13. Monitoring of 4-ATP dimerization via *operando* SERS on Au SCs. a) Schematic representation of the reaction at the surface of an Au SC. b) Photocatalytic activities of the Au SCs depending on the relative disposition with respect to the substrate and under *operando* SERS. Irradiation conditions: λexc: 633 nm, 100x obj., 0.25 mW power + 0.5 s acquisition time.

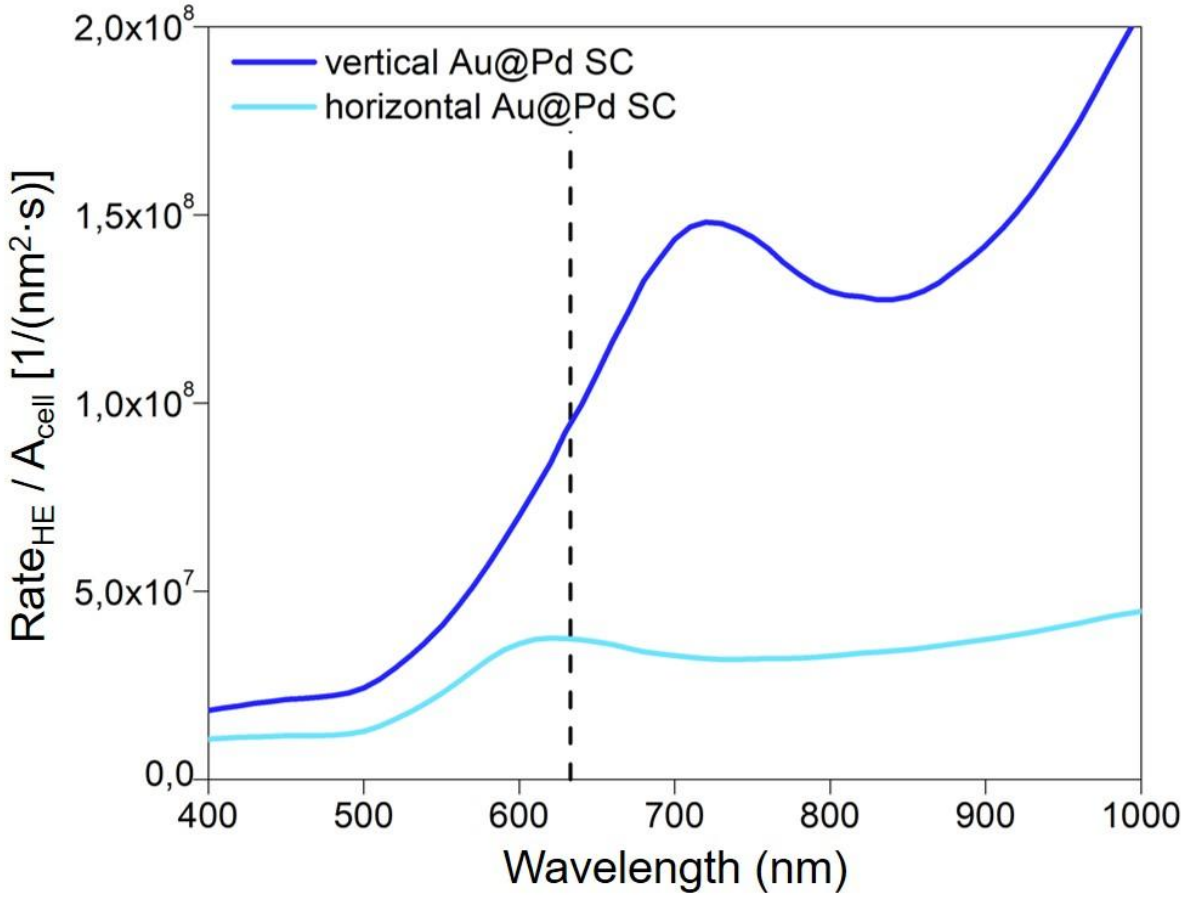

Figure S14. Calculated populations of hot electrons obtained from the integration of the entire surface of the Au@Pd NRs within the SC. The line represents the irradiation wavelength of the laser in the SERS experiments.

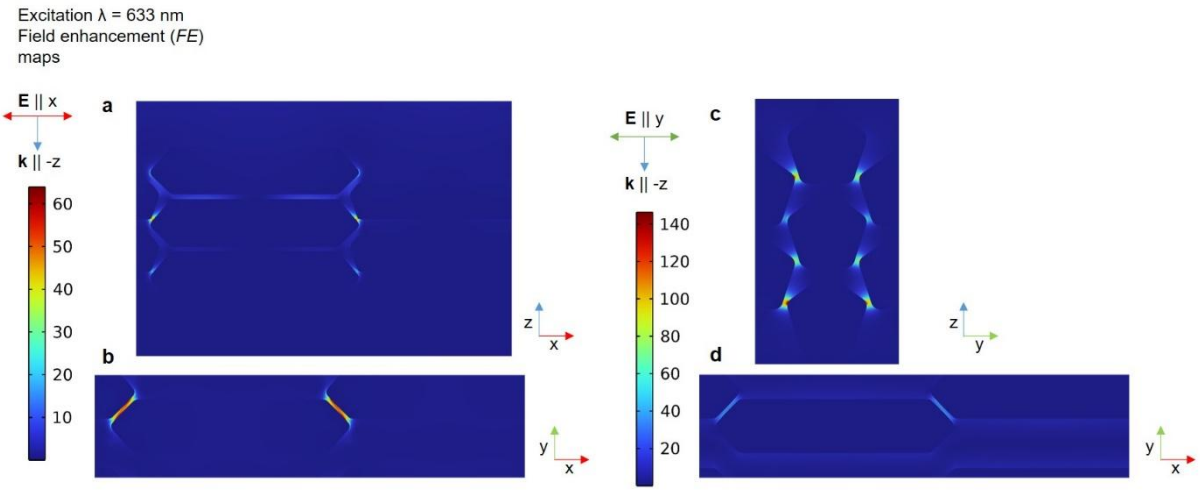

Figure S15. (a-d) Electromagnetic field enhancement maps for the 5-layer horizontal array of Au@Pd NRs. The wavevector k indicates the propagation direction of the incoming linearly-polarized planewave, with electric field E (a-b: polarized along the x-axis; c-d: polarized along the y-axis). b, d) The xy planes are taken at a $|\Delta z|$ = 23 nm from the top point of the top layer. The axes indicated as insets show the orientation of the cross-sectional maps.

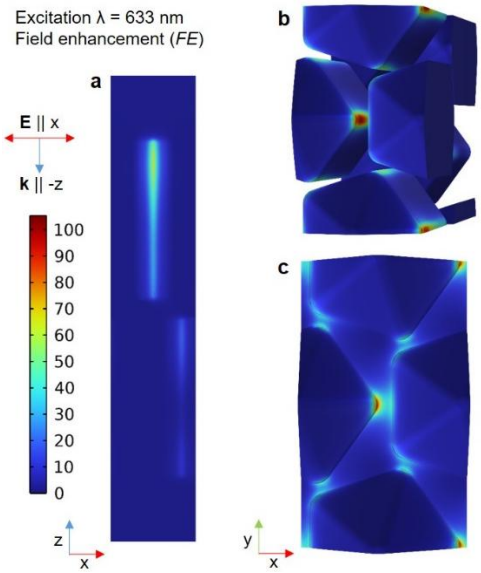

Figure S16. (a-c) Electromagnetic field enhancement maps for the 2-layer vertical array of Au@Pd NRs. The wavevector k indicates the propagation direction of the incoming electric field E (polarized along the x-axis). c) The xy plane is took at $|\Delta z|$ = 13 nm from the top point of the top layer. The axes indicated as insets show the orientation of the cross-sectional maps.

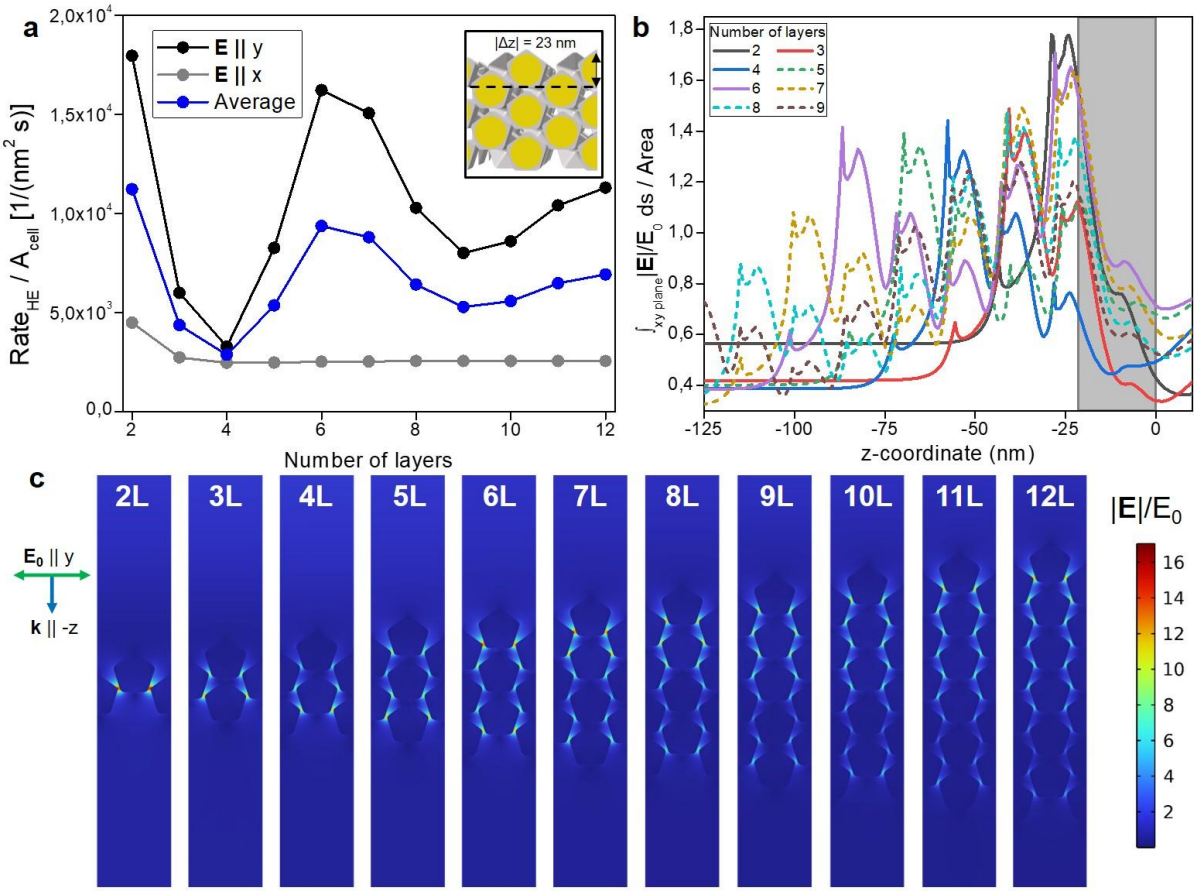

Figure S17. a) Surface-averaged rate of hot electrons ($Rate_{HE}$) for Au@Pd SCs with different number of layers of horizontally-oriented NRs (A_{cell}: area of the horizontal section of the unit cell). The excitation wavelength is 633 nm. Inset: Penetration depth used for the calculation of the surface-averaged $Rate_{HE}$ shown in panel. b) Spatial evolution of the surface integration in a XY-plane of the magnitude $|E|/E_0$ along the z-axis, normalized by the integrating area. The incident wave is polarized along the y-axis and has a wavelength of 633 nm. The shaded area corresponds to the z-coordinate values at which we are computing the $Rate_{HE}$ on the surface of the Pd layer. c) $|E|/E_0$ maps for the supercrystal deposited parallel to the substrate for a different number of layers. The incident wave is polarized along the y-axis and has a wavelength of 633 nm.

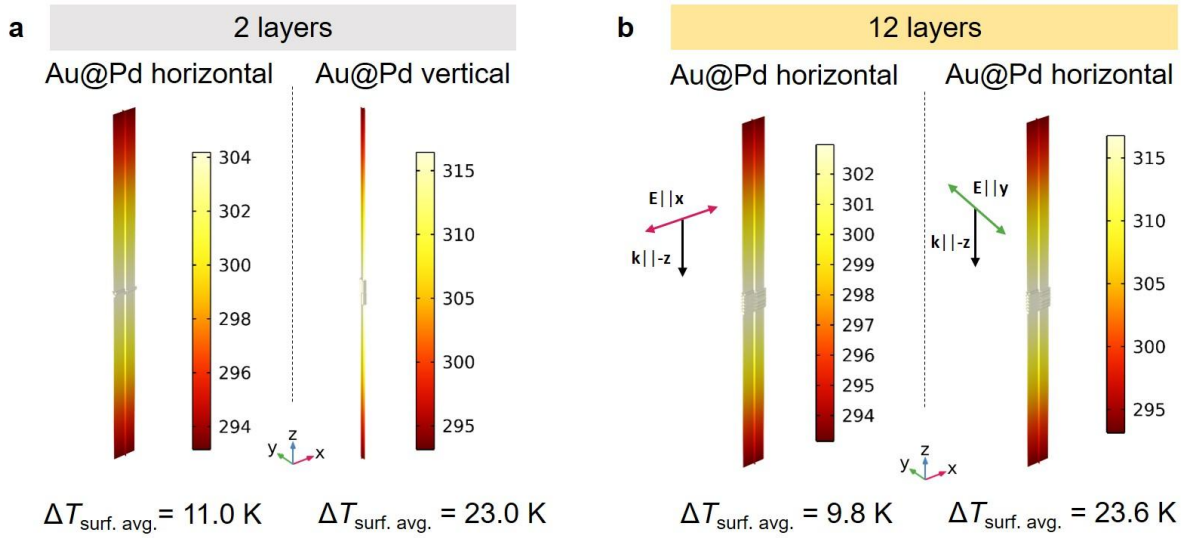

Figure S18. a) Temperature maps and temperature differences with respect to T_{room} = 293.15 K of periodic horizontal and vertical supercrystal configurations, sharing the same number of rods per unit cell (n = 4), immersed in air, achieved for the steady state solution of the heat diffusion equation, under planewave illumination with a I_0= 130 W/cm^2 and a wavelength of 633 nm, averaged over two orthogonal linear polarizations. b) Temperature maps for Au@Pd horizontal supercrystals with 12 layers of structures, disaggregating the two perpendicular linear polarizations. With other parameters remaining constant, reaching the local temperature achieved by two layers of vertically arranged rods would require increasing the number of layers and using light linearly polarized alongside the long axis of the rods.

References

[1] A. Sánchez-Iglesias, N. Winckelmans, T. Altantzis, S. Bals, M. Grzelczak, L. M. Liz-Marzán, *J. Am. Chem. Soc.* **2017**, *139*, 107.

[2] A. Sánchez-Iglesias, K. Jenkinson, S. Bals, L. M. Liz-Marzán, *J. Phys. Chem. C* **2021**, *125*, 23937.

[3] S. Rodal-Cedeira, V. Montes-García, L. Polavarapu, D. M. Solís, H. Heidari, A. La Porta, M. Angiola, A. Martucci, J. M. Taboada, F. Obelleiro, S. Bals, J. Pérez-Juste, I. Pastoriza-Santos, *Chem. Mater.* **2016**, *28*, 9169.

[4] P. B. Johnson, R. W. Christy, *Phys. Rev. B* **1972**, *6*, 4370.

[5] P. B. Johnson, R. W. Christy, *Phys. Rev. B* **1974**, *9*, 5056.

[6] L. V. Besteiro, X. T. Kong, Z. Wang, G. Hartland, A. O. Govorov, *ACS Photonics* **2017**, *4*, 2759.

[7] E. Y. Santiago, L. V. Besteiro, X. T. Kong, M. A. Correa-Duarte, Z. Wang, A. O. Govorov, *ACS Photonics* **2020**, *7*, 2807.

[8] Y.-F. Huang, H.-P. Zhu, G.-K. Liu, D.-Y. Wu, B. Ren, Z.-Q. Tian, *J. Am. Chem. Soc.* **2010**, *132*, 9244.

[9] J. Kim, X. Song, F. Ji, B. Luo, N. F. Ice, Q. Liu, Q. Zhang, Q. Chen, *Nano Lett.* **2017**, *17*, 3270.

[10] J. P. Pouget, M. E. Józefowicz, A. J. Epstein, X. Tang, A. G. MacDiarmid, *Macromolecules* **1991**, *24*, 779.

[11] Y. Negrín-Montecelo, C. Brissaud, J. Y. Piquemal, A. O. Govorov, M. A. Correa-Duarte, L. V. Besteiro, M. Comesaña-Hermo, *Nanoscale* **2022**, *14*, 11612.